aerospace

MDPI

*Article*

# Aero-Propulsive-Elastic Coupled Modeling of Distributed Electric Propulsion Systems with Slipstream Interactions

**Jun Wei [1], Wei Gao [2], Bei Lu [1] and Qifu Li [1,*]**

[1] School of Aeronautics and Astronautics, Shanghai Jiao Tong University, Shanghai 200240, China; weijunsjtu@sjtu.edu.cn (J.W.); beilu@sjtu.edu.cn (B.L.)
[2] AECC Hunan Aviation Powerplant Research Institute, Zhuzhou 412002, China; willgao@alumni.sjtu.edu.cn
* Correspondence: qifuli@sjtu.edu.cn

**Abstract**

The distributed electric propulsion (DEP) system offers significant potential for enhancing aerodynamic efficiency, reducing emissions, and enabling innovative aerodynamic configurations. However, the strong coupling between propeller slipstream effects and wing structural dynamics presents new challenges for aeroelastic analysis. To address this issue, this paper proposes an aeroelastic modeling approach tailored for DEP systems that systematically accounts for the effects induced by propeller slipstreams. Specifically, the induced velocity generated by the propeller slipstreams is computed using a slipstream tube model and incorporated into the unsteady aerodynamic modeling via the unsteady vortex lattice method. Under appropriate assumptions, a state-space formulation of the unsteady aerodynamic forces is derived, while the wing structural dynamics are represented using the finite element method. After establishing the subsystem models, a complete aeroelastic model of the DEP system is assembled based on the input–output relationships among the subsystems. Nonlinear simulations are conducted using this integrated model. The results demonstrate the potential of distributed propellers for suppressing wing vibrations and alleviating structural loads.

**Keywords:** distributed electric propulsion; aeroelasticity; slipstream effects; slipstream tube model; unsteady vortex lattice method

## 1. Introduction

The impact of greenhouse gas emissions and the historical volatility of fossil fuel costs has driven extensive research in the aerospace community, aiming to develop propulsion systems that outperform current state-of-the-art technologies in terms of energy efficiency and carbon emissions [1,2]. To meet the demands for high economic performance, low energy consumption, low noise, and minimal environmental impact, distributed electric propulsion (DEP) systems have increasingly been recognized as a key enabling technology for improving propulsion efficiency and performance [3–5]. As a core technology for next-generation aerospace systems, DEP deploys multiple small electric propulsors across the wing or fuselage, enabling integrated design with wing structures and other subsystems [6,7]. This integrated design approach offers multiple advantages: noise reduction due to ground shielding effects of the propulsion units or the inherently lower noise of electric motors compared to gas turbines [8,9], enhanced safety through redundancy provided by the increased number of propulsion units [10], and efficiency gains arising from aerodynamic–propulsion coupling effects, such as boundary-layer ingestion to improve

Check for updates

Academic Editor: Angel Velazquez

Received: 12 May 2026
Revised: 1 July 2026
Accepted: 2 July 2026
Published: 4 July 2026

**Copyright:** © 2026 by the authors. Licensee MDPI, Basel, Switzerland. This article is an open access article distributed under the terms and conditions of the Creative Commons Attribution (CC BY) license.

propulsive efficiency or wake filling to reduce kinetic energy losses [11–14]. Furthermore, distributing multiple electric motors along the wing span provides the potential to actively or passively mitigate wing loads through favorable aeroelastic responses [15].

Due to the distributed arrangement of electric motors, which necessitates the use of a high-aspect-ratio wing configuration, combined with the application of advanced composite materials, the structural flexibility of the wing is increased [16]. Wings may experience substantial structural deformation or exhibit vibratory responses when subjected to disturbances. Under such conditions, although simplifying the wing as a rigid body for modeling purposes is straightforward, the coupling effects between structural deformation and aerodynamic characteristics cannot be neglected in realistic models. In DEP systems, the structural flexibility of the wing becomes an important factor that cannot be ignored. At the same time, the influence of propeller slipstreams on the elastic response is equally significant. Consequently, extensive research has been conducted over the years to investigate both the slipstream effects in DEP configurations and the aeroelastic modeling of flexible wings.

In studies of slipstream effects on DEP systems, propeller-induced slipstreams can alter the local flow field over the wing, thereby affecting the lift distribution. The strong coupling between these slipstream effects and wing aerodynamics presents significant challenges for the aerodynamic modeling of DEP systems. Prandtl made pioneering contributions to the study of propeller–wing interactions. He analyzed the effects of propeller slipstream on airfoil aerodynamics using experimental methods. The results showed that the airfoil is primarily influenced by changes in flow velocity, while variations in flow direction also significantly affect drag, especially when the airfoil is outside the slipstream. Since Prandtl's work, many researchers have employed experimental methods to investigate this topic. Marcus [17] et al. conducted wind tunnel tests with a single propeller mounted on a wing with a Fowler flap, varying chordwise position and inclination. Results showed significant bidirectional aerodynamic coupling, with lift increases of 8% at cruise and 3% at high-lift conditions when the propeller was mounted on the flap. Sinnige [18] et al. investigated the aerodynamics of wingtip-mounted propellers. Wind tunnel tests at Delft University of Technology using particle image velocimetry (PIV), surface-pressure, and balance measurements showed that wingtip propellers reduce induced drag by attenuating wingtip vortices, achieving 15% drag reduction at a lift coefficient of 0.5 and thrust coefficient of 0.12. The benefit increases with higher lift and thrust, mainly due to improved wing span efficiency. De Vries [19] et al. mounted a propeller above the hinge line of a wing with a trailing-edge flap and measured the flow using pressure taps, microphones, and PIV. Results showed that the propeller-induced adverse pressure gradient increases with thrust and can cause hinge-line flow separation, while moving the propeller upstream by half a radius induces a Coandă effect that maintains attachment.

To gain deeper insight into the slipstream-induced aerodynamic interactions between propellers and wings, numerical methods are commonly employed to analyze complex distributed-propeller wing configurations. In the initial stages, simple low-fidelity numerical approaches are used to estimate the effects of the propellers on the wing. Herzog [20] et al. proposed a distributed electric propulsion layout for CS23 turboprop aircraft, using a blade element vortex lattice method for aerodynamic trim and adjusting wing chord and propeller blade parameters to satisfy force balance, and compared the propulsive efficiency and power consumption of different configurations. Raichle [21] developed a novel discretization method combining blade element theory and the actuator disk model for frictionless, incompressible axial propeller–wing flows, proposed a lift and drag calculation accounting for blade rotation, and integrated the method into the TAU flow solver at the German Aerospace Center. With the increase in computational power, many studies

have employed Reynolds-Averaged Navier–Stokes (RANS) simulation to quantify specific aerodynamic interference phenomena in propeller–wing configurations. De Rosa [22] et al. studied the aerodynamic effects of distributed electric propulsion on a regional aircraft using a high-fidelity computational fluid dynamics (CFD) method. They analyzed different propeller diameters and thrust levels on a finite-span wing with periodic boundary conditions, quantified aerodynamic coefficient gains relative to the power-off case, and proposed a simplified analytical model for preliminary design. Della Vecchia [23] studied the aerodynamic effects of mid-wing and wingtip-mounted propellers using a CFD virtual disk model. Results show that wingtip propellers reduce induced drag, while distributed propellers enhance high-lift performance, lowering induced drag by 2–3% at low cruise lift and 8–10% at high cruise lift, and increasing maximum lift coefficient by 20–30% in clean and over 50% in flapped configurations.

When the elastic deformation of the wing is within a small range, its structural behavior can be approximated as geometrically linear [24]. Under this assumption, the wing in the DEP system is modeled as a flexible structure whose deformation remains within the linear elastic range [25,26]. However, even when the deformation amplitude is small, flexible wings still exhibit elastic responses under aerodynamic loads, leading to aeroelastic coupling between aerodynamic forces and structural responses [27]. Therefore, integrated modeling of structural dynamics and aeroelasticity is essential for flexible wings. Zúñiga [28] et al. investigated a composite UAV with a 4 m wingspan and an aspect ratio of 18.9. They performed conventional aerodynamic analysis using the vortex lattice method and developed a flexible flight dynamics model based on the approach of Waszack and Schmidt [29], incorporating ground vibration test modes. The study examined the effects of wing flexibility and tail aerodynamics on aeroelasticity and flight dynamics. Guo [30] et al. addressed the flexible deformation of high-aspect-ratio wings in a solar-powered UAV by developing a coupled model of flexible wings and a rigid fuselage, integrating s-beam structural modeling, finite-state induced flow aerodynamics, engine static/dynamic modeling, and rigid-body flight dynamics, with structural parameters refined using flight data. Simulations show that, compared with the rigid model, the coupled model exhibits significant lag, with motion amplitude reduced by 50%, frequency by 15%, kinetic energy by 11.8%, and elevator control efficiency by over 40%. Guimarães [31] et al. developed and applied a low-speed aeroelastic flight dynamics model within the University of Michigan/High-Speed Vehicle framework to simulate supersonic aircraft at high angles of attack. The model captures dominant vortex structures, unsteady effects, and structural flexibility. Using the supersonic configurations of low-speed baseline aircraft, results show its suitability for parametric studies, optimization constraint generation, and providing adequate dynamics and handling qualities during climb and descent maneuvers. Beyer [32] et al. developed a simulation environment for gust load alleviation (GLA) in energy-efficient passenger aircraft. The model combines indicial functions with a dynamic stall model for unsteady aerodynamics, uses a nonlinear steady lifting-line method for downwash, and couples structural dynamics via modal displacement. Validation against unsteady RANS shows good agreement. Results demonstrate open-loop gust load envelopes for a lightweight wing designed by reducing limit loads from 2.5 g to 2.0 g, providing a basis for parametric studies of GLA controllers and flow actuators.

Current research on the aeroelasticity of DEP systems has primarily focused on identifying stability boundaries and analyzing the destabilizing nature of propeller–wing interactions. Böhnisch [33] et al. developed a mid-fidelity propeller–wing aeroelastic model based on DUST and MBDyn to investigate the effects of aerodynamic interactions on flutter characteristics. Their results indicated that the propeller–wing aerodynamic interaction slightly destabilizes the system, reducing the flutter speed by approximately 5%, with the thrusting

condition exhibiting a more pronounced destabilizing effect than the windmilling condition. Wu [34] et al. developed a rapid nonlinear aeroelastic framework for highly flexible wings with distributed propellers and investigated the effects of thrust and slipstream on the dynamic response and aeroelastic stability. Their results showed that thrust suppresses vibration and increases the flutter boundary, whereas slipstream exerts a destabilizing effect by increasing local dynamic pressure and lift. The study highlighted the potential of distributed propellers for gust alleviation and flutter suppression in highly flexible aircraft. Sun [35] et al. developed a static aeroelastic analysis framework for a distributed propulsion wing (DPW) based on a loosely coupled CFD/CSD approach. The framework integrates the RANS momentum source method with a finite-element structural model, and employs a three-dimensional radial basis function interpolation method for aerodynamic–structural data transfer. The results indicate that the static aeroelastic deformation of the DPW is dominated by bending and positive torsion, and that slipstream effects significantly influence the lift distribution and longitudinal static stability. In addition, an equivalent airfoil-based method is proposed for efficient engineering-level analysis. However, leveraging the distributed characteristics of the propulsion system for active structural response regulation remains limited. Considering the characteristics of DEP systems, the slipstreams generated by multiple propellers alter the local flow field over the wing [36,37], thereby complicating the lift distribution. The slipstream-induced velocities are strongly coupled with the flexible wing structure, resulting in nonlinear aeroelastic interactions. Due to the high coupling among aerodynamics, structure, and propulsion, an integrated aero–propulsion–structure modeling approach is required. Furthermore, high-fidelity methods are computationally expensive, while low-order models often lack sufficient accuracy, making the trade-off between efficiency and precision a key challenge. This study proposes a computationally efficient state-space aeroelastic model. The framework not only incorporates slipstream–wing coupling effects but also validates the feasibility of leveraging propeller-induced effects for the regulation of wing structural responses. Consequently, it transforms distributed propellers from a potential source of instability into a proactive asset for active control.

In this paper, a DEP system with a configuration similar to the NASA X-57 [38,39] is considered as a case study. Figure 1 illustrates a schematic diagram of the DEP system and the wing deformation induced by the reaction torque of distributed propellers. The aeroelastic modeling assumes linear structural vibrations. For the aerodynamic model, a compromise between accuracy and computational efficiency is achieved by employing a three-dimensional unsteady vortex lattice method (UVLM) based on potential flow theory [40], which enables efficient modeling and optimization of lifting surfaces in distributed electric propulsion systems. Aerodynamic states are introduced to capture unsteady effects and describe the dynamic behavior of aerodynamic forces under varying boundary conditions. To facilitate subsequent model integration, the aerodynamic module is formulated in a state-space representation. A numerical slipstream tube model (STM) [37,41] is used to analyze aerodynamic interactions between the wing and distributed propellers, which is then coupled into the UVLM state-space equations to construct a wing aerodynamic model accounting for slipstream effects. For structural modeling, finite element methods are employed to obtain wing structural parameters. These results are subsequently used to establish the structural dynamic equations of the distributed electric propulsion system. Data exchange between the structural and aerodynamic models is performed via infinite plate spline interpolation [42]. Figure 2 illustrates a schematic diagram of the aeroelastic modeling of a distributed electric propulsion system. This study addresses the strong coupling between propeller slipstream and wing structural dynamics in the DEP system, and proposes an aeroelastic modeling approach capable of systematically characterizing slipstream effects. The method integrates the STM with the UVLM and

couples them with a finite-element structural model to construct a unified aerodynamics–structure–propulsion framework.

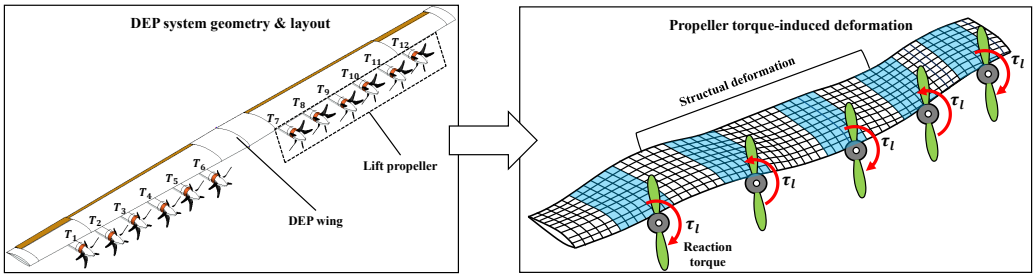



**Figure 1.** Schematic of the DEP system and illustration of propeller reaction torque-induced deformation.

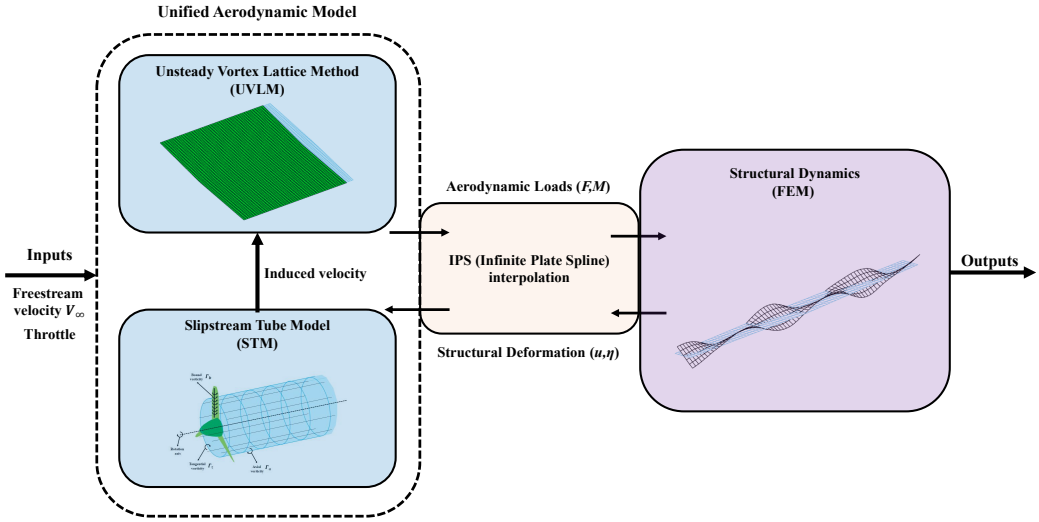



**Figure 2.** Schematic diagram of the aeroelastic model of a DEP system.

The paper is organized as follows: Section 2 develops the aerodynamic model for the DEP system based on the unsteady vortex lattice method, taking into account the effects of propeller slipstreams. Section 3 establishes the structural dynamics model of the DEP system. Section 4 integrates the aerodynamic and structural dynamics models to construct the full aeroelastic model of the DEP system. Section 5 presents the results of nonlinear simulations. Finally, Section 6 concludes the paper.

## 2. Aerodynamic Modeling Based on the Unsteady Vortex Lattice Method

Aerodynamic modeling constitutes a fundamental basis for the dynamic analysis of DEP systems. In such systems, the flexible structural deformations of the wing interact with aerodynamic forces, resulting in complex dynamic coupling whose effects cannot be neglected. To more accurately capture the instantaneous variations of aerodynamic forces induced by atmospheric conditions and flexible-structure vibrations, it is necessary to incorporate unsteady effects in the aerodynamic modeling process.

In this section, based on potential flow theory [43], vortex rings are employed as the fundamental units for aerodynamic modeling, and the application of the UVLM in the analysis of DEP systems is investigated. The primary reason for selecting the UVLM is its ability to capture the unsteady aerodynamic effects on lifting surfaces, as well as its convenient coupling with the structural model and the STM. An extension from discrete-time step formulations to a state-space representation is considered, providing a more

general and computationally efficient framework for unsteady aerodynamic modeling, serving as a foundation for the aerodynamic analysis of DEP systems.

STM is employed to obtain the induced velocity of distributed propeller slipstreams at the aerodynamic grid control points of the wing. This induced velocity is treated as the input to the wing aerodynamic state-space model, thereby integrating the propeller slipstream effects with the wing aerodynamic surfaces to yield an aerodynamic model of a DEP system that accounts for propeller slipstream effects.

### *2.1. Unsteady Vortex Lattice Method*

In this study, the UVLM [44,45] is employed to model the aerodynamic loads. The lifting surface is discretized into a grid of $M \times N$ rectangular panels. Based on the thin-airfoil theory, each panel contains a bound vortex ring with a constant circulation $\Gamma_j$ $(j = 1, \ldots, M \times N)$. As illustrated in Figure 3, the leading-edge segment of each vortex ring is placed at the panel's quarter-chord position, while the control point is located at the three-quarter chord position to enforce the boundary conditions.

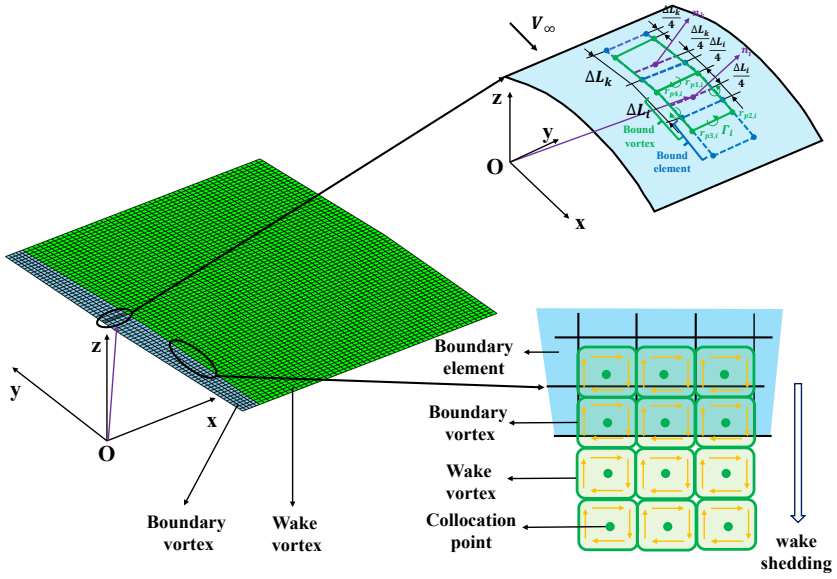



**Figure 3.** The sketch of the vortex ring elements.

The kinematic boundary condition requires that the net normal velocity at each control point must be zero. At each time step $t$, the flow tangency condition for the $i$-th panel is expressed as:

$$\sum_{j=1}^{M\times N} A_{ij}\Gamma_j^{(t)} + (\boldsymbol{V}_{ind,w,i} + \boldsymbol{V}_{\infty,i} + \boldsymbol{V}_{m,i}) \cdot \boldsymbol{n}_i = 0 \tag{1}$$

where $A_{ij}$ is the aerodynamic influence coefficient (AIC) matrix, representing the normal velocity induced by a unit-strength vortex ring $j$ at control point $i$. $\boldsymbol{V}_{ind,w,i}$ denotes the velocity induced by the entire wake system, $\boldsymbol{V}_{\infty,i}$ is the freestream velocity, and $\boldsymbol{V}_{m,i}$ is the grid's local kinematic velocity, which includes translation, rotation, and elastic deformation. The unit normal vector at the $i$-th control point is denoted by $\boldsymbol{n}_i$.

The induced velocity generated by any straight vortex segment (extending from $\boldsymbol{r}_1$ to $\boldsymbol{r}_2$ with strength $\Gamma$) acting on a point $\boldsymbol{r}_p$ is calculated using the discrete Biot–Savart law. To mitigate numerical singularities, the Scully vortex core model [46] is applied:

$$\boldsymbol{v} = \frac{\Gamma}{4\pi} \frac{\boldsymbol{r}_1 \times \boldsymbol{r}_2}{\|\boldsymbol{r}_1 \times \boldsymbol{r}_2\|^2 + r_c^4} \left( \frac{\boldsymbol{r}_1 \cdot (\boldsymbol{r}_2 - \boldsymbol{r}_1)}{\|\boldsymbol{r}_1\|} - \frac{\boldsymbol{r}_2 \cdot (\boldsymbol{r}_2 - \boldsymbol{r}_1)}{\|\boldsymbol{r}_2\|} \right) \tag{2}$$

where vectors $\boldsymbol{r}_1$ and $\boldsymbol{r}_2$ are defined relative to $\boldsymbol{r}_p$, and $r_c$ denotes the regularization radius.

The unsteady wake is modeled using a time-stepping free-wake procedure (Figure 4). At the end of each time step, a new row of wake elements is shed from the trailing edge. The strength of the newly shed vortex $\boldsymbol{\Gamma}_{w,0}$ is determined by the unsteady Kutta condition, ensuring the conservation of circulation: $\boldsymbol{\Gamma}_{w0}^{(t+1)} = \boldsymbol{\Gamma}_{TE}^{(t)}$. Simultaneously, the geometry of the entire wake is updated by convecting the wake vertices $\boldsymbol{X}_w$ with the local flow velocity:

$$\boldsymbol{X}_w^{t+1} = \boldsymbol{X}_w^t + (\boldsymbol{V}_\infty + \boldsymbol{v}_{ind}^t)\Delta t \tag{3}$$

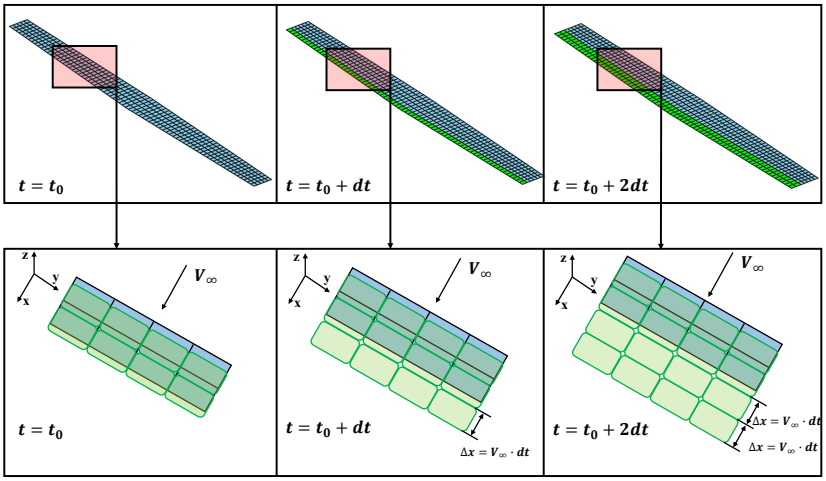



**Figure 4.** The sketch of vortex shedding and transport.

Once the circulation distribution is solved, the aerodynamic force $\boldsymbol{F}$ on each bound vortex segment is computed using the unsteady Kutta–Joukowski theorem [47]. The force is decomposed into steady (circulatory) and unsteady (added mass) components:

$$\boldsymbol{F} = \rho\boldsymbol{\Gamma}(\boldsymbol{V} \times d\boldsymbol{l}) + \rho\frac{\partial \boldsymbol{\Gamma}}{\partial t}c(\hat{\boldsymbol{V}} \times d\boldsymbol{l}) \tag{4}$$

where $\rho$ is the fluid density, $\boldsymbol{V}$ is the local flow velocity, and $\mathrm{d}\boldsymbol{l}$ is the increment of the vortex vector. The unit vector of the local flow velocity is defined as $\hat{\boldsymbol{V}} = \boldsymbol{V}/\|\boldsymbol{V}\|$. The scalar $c$ represents the length of the vortex segment, and the unsteady component is related to the rate of change of the vortex strength, $\frac{\partial \boldsymbol{\Gamma}}{\partial t}$. The total aerodynamic forces and moments are obtained by integrating these contributions over all bound vortex segments.

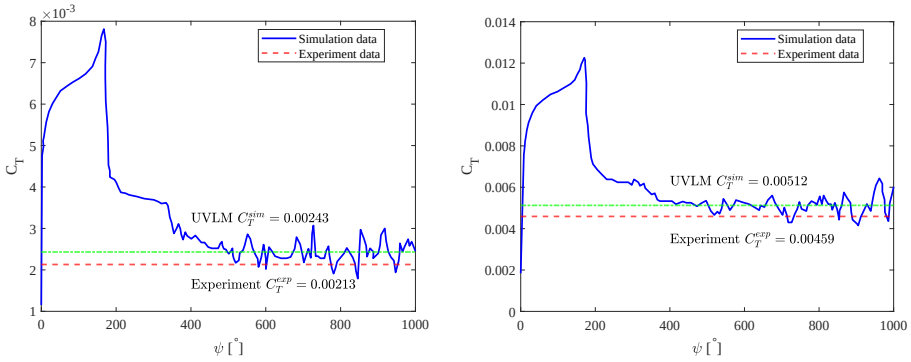
To verify the accuracy of the UVLM numerical model code in this study, a comparison was conducted using the two-bladed hovering case reported in References [48–50]. The model rotor consists of 2 rectangular, untwisted and untapered NACA0012 rigid blades. The blade geometric parameters and operating conditions are defined in Table 1. The aerodynamic mesh of each blade consists of $M \times N = 20 \times 10$ boundary elements. Figure 5 and Table 2 present the variations of thrust coefficient $C_T$ with blade azimuth angle $\psi$ for angles of attack $\alpha$ of 5° and 8°. The green dashed line represents the mean steady-state convergence value of the UVLM. It can be observed that, although the thrust coefficient predicted by the UVLM exhibits a trend consistent with the experimental data, its steady-state mean value is approximately 15% higher. This discrepancy is mainly attributed to the inability of potential flow theory to account for the decambering effect induced by the viscous boundary layer, as well as the local flow separation occurring near the blade root.

Figure 6 illustrates the evolution of the blade wakes. When the rotor reaches a half-revolution, each blade gradually approaches the starting vortex generated by the other blade, at which point the thrust coefficient rises and reaches its maximum. Subsequently, when the blade encounters the starting vortex and the wakes overlap, the thrust coefficient

suddenly drops. As the system continues to evolve, this wake interaction gives rise to complex local flow conditions, and the typical singularity problems associated with the Biot–Savart law become evident, leading to numerical instabilities. The observed wake evolution is generally consistent with that reported in reference [50].

**Table 1.** Geometric and operational parameters of the propeller.

| Parameter | Value |
|---|---|
| Chord length $c$ | 0.16 m |
| Blade external radius $R$ | 1.143 m |
| Aspect ratio $AR$ | 8 |
| Rotational speed $\omega$ | 1250 rpm |
| Angle of attack $\alpha$ | 5° and 8° |

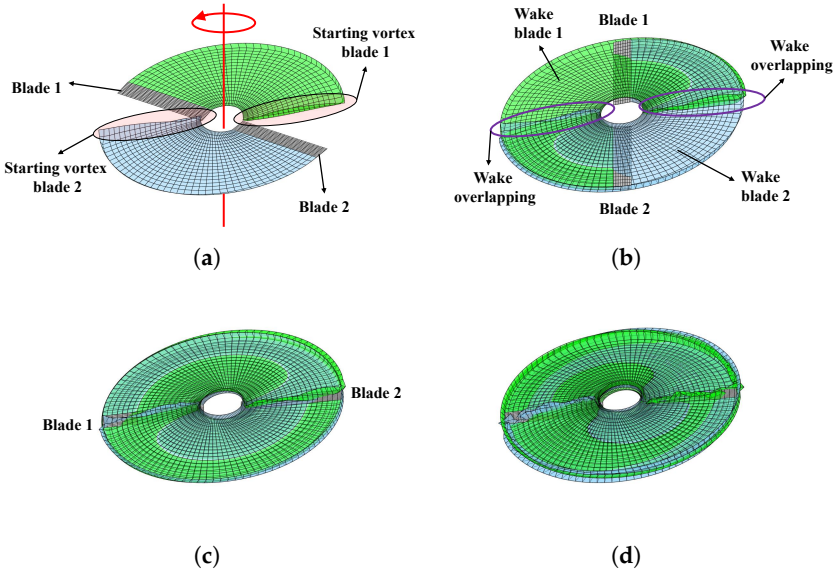



(**a**) $\alpha = 5°$ (**b**) $\alpha = 8°$

**Figure 5.** The variation of the thrust coefficient with the blade azimuth angle $\psi$ under different angles of attack.

**Table 2.** Thrust coefficient comparison between experiment and UVLM.

| Angle of Attack [°] | Experiment [50] | UVLM | Relative Error [%] |
|---|---|---|---|
| 5 | 0.00213 | 0.00243 | 14.1 |
| 8 | 0.00459 | 0.00512 | 11.5 |




(**a**) (**b**)

(**c**) (**d**)

**Figure 6.** (**a**–**d**) Evolution of the blade wakes.

To assess the capability of UVLM in simulating propeller–wing interactions, the PROWIM experiment conducted by Veldhuis [51] was simulated. The experimental setup consists of a straight wing with an aspect ratio of 5.33, a symmetric NACA 642-A015 airfoil, and a wingspan of 1.28 m, with a Beaver propeller mounted at 46.9% of the wingspan from the fuselage centerline. Figure 7 shows a schematic diagram of the geometric parameters of the Beaver propeller. The freestream velocity was $V_\infty = 49.5$ m/s, corresponding to an advance ratio of $J = 0.85$. Figure 8 presents the spanwise lift distribution at zero angle of attack, showing that the UVLM predictions in this study closely match the experimental measurements.

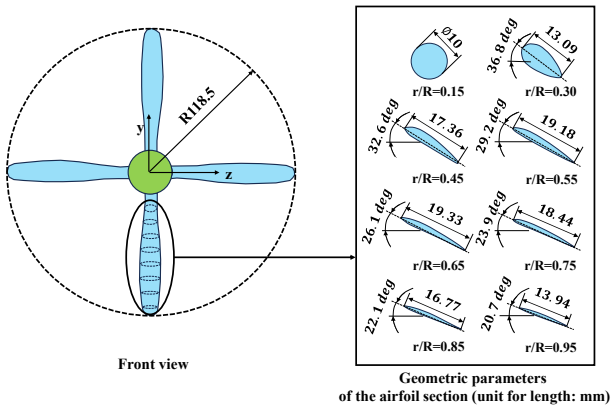



**Figure 7.** Schematic diagram of the geometric parameters of the Beaver propeller.

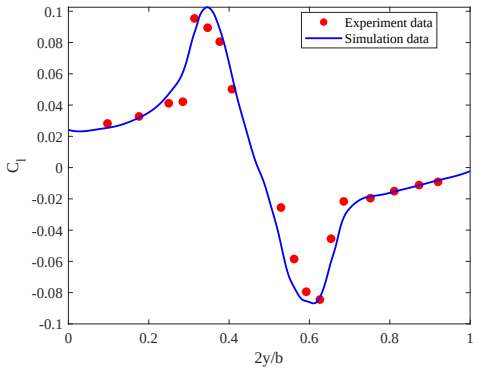



**Figure 8.** Spanwise lift distribution of the wing.

### *2.2. Aerodynamic State-Space Model Based on UVLM*

In unsteady aerodynamic modeling, aerodynamic states are introduced to describe the dynamic behavior of aerodynamic forces under varying boundary conditions. For ease of subsequent model integration, the aerodynamic module can be formulated in a state-space representation [52]. Within the UVLM framework, by linearizing the time-marching formulation of the UVLM under the small-perturbation assumption, a state-space unsteady aerodynamic model valid in the vicinity of the considered flight condition can be obtained.

Assuming small perturbations and sufficiently small time steps, the deformation of the trailing vortices can be neglected, and the wake vortex strength variation rate can be approximated by finite differences, as given by the following expression:

$$\dot{\boldsymbol{\Gamma}}_{w1}^{t} = \frac{\boldsymbol{\Gamma}_{w1}^{t+1} - \boldsymbol{\Gamma}_{w1}^{t}}{\Delta t} = \frac{(\boldsymbol{W}_1 - \boldsymbol{I})\boldsymbol{\Gamma}_{w1}^{t} + \boldsymbol{W}_2\boldsymbol{\Gamma}_{w0}^{t}}{\Delta t} \tag{5}$$

where $\boldsymbol{\Gamma}_{w1}^{t+1} = \boldsymbol{W}_1\boldsymbol{\Gamma}_{w1}^{t} + \boldsymbol{W}_2\boldsymbol{\Gamma}_{w0}^{t}$, $\boldsymbol{\Gamma}_{w1}$ denotes the wake vortex strengths from the second row onward, $\boldsymbol{\Gamma}_{w0}$ denotes the wake vortex strengths of the first row, and $\boldsymbol{W}_1$ and $\boldsymbol{W}_2$ are

coefficient matrices used to define the convection of the wake. In order to establish the relationship between the wake vortex and the bound vortex, Equation (1) is rewritten in the following form:

$$\boldsymbol{A}_{bb}\boldsymbol{\Gamma}_b + \boldsymbol{A}_{bw0}\boldsymbol{\Gamma}_{w0} + \boldsymbol{A}_{bw1}\boldsymbol{\Gamma}_{w1} = \boldsymbol{w}_j \tag{6}$$

where $\boldsymbol{A}_{bw0}$ denotes the aerodynamic influence matrix of the first-row wake vortices on the bound vortices, while $\boldsymbol{A}_{bw1}$ represents the aerodynamic influence matrix of the second-row and subsequent wake vortices on the bound vortices, and $\boldsymbol{w}_j$ denotes the downwash velocity on the wing surface. the Kutta condition can also be rewritten in the following form:

$$\boldsymbol{W}_3\boldsymbol{\Gamma}_b + \boldsymbol{W}_4\boldsymbol{\Gamma}_{w0} = 0 \tag{7}$$

where $\boldsymbol{W}_3$ and $\boldsymbol{W}_4$ denote the coefficient matrices for the transfer from the bound vortices to the first-row wake vortices. Substituting Equations (6) and (7) into Equation (5) yields the following state-space equation:

$$\dot{\boldsymbol{\Gamma}}_{w1} = \boldsymbol{A}_w\boldsymbol{\Gamma}_{w1} + \boldsymbol{B}_w\boldsymbol{w}_j \tag{8}$$

where

$$\begin{aligned} \boldsymbol{A}_w &= \frac{1}{\Delta t}\left[(\boldsymbol{W}_1 - \boldsymbol{I}) - \boldsymbol{W}_2(\boldsymbol{W}_4 - \boldsymbol{W}_3\boldsymbol{A}_{bb}^{-1}\boldsymbol{A}_{bw0})^{-1}\boldsymbol{W}_3\boldsymbol{A}_{bb}^{-1}\boldsymbol{A}_{bw1}\right] \\ \boldsymbol{B}_w &= -\frac{1}{\Delta t}\boldsymbol{W}_2(\boldsymbol{W}_4 - \boldsymbol{W}_3\boldsymbol{A}_{bb}^{-1}\boldsymbol{A}_{bw0})^{-1}\boldsymbol{W}_3\boldsymbol{A}_{bb}^{-1} \end{aligned} \tag{9}$$

The unsteady aerodynamic calculation based on Equation (4) can be rewritten in the following form:

$$\boldsymbol{F}_a = \boldsymbol{F}_{a,st} + \boldsymbol{F}_{a,unst} = \boldsymbol{L}_1\boldsymbol{\Gamma}_b + \boldsymbol{L}_2\dot{\boldsymbol{\Gamma}}_b \tag{10}$$

where $\boldsymbol{L}_1$ and $\boldsymbol{L}_2$ are the coefficient matrices corresponding to the steady and unsteady terms, respectively. By substituting Equations (6) and (7) into Equation (10), the aerodynamic output equation can be expressed as follows:

$$\boldsymbol{F}_a = \begin{bmatrix}\boldsymbol{L}_1 & \boldsymbol{L}_2\end{bmatrix}\left(\begin{bmatrix}\boldsymbol{L}_4 \\ \boldsymbol{L}_4\boldsymbol{A}_w\end{bmatrix}\boldsymbol{\Gamma}_{w1} + \begin{bmatrix}-\boldsymbol{L}_3 & \boldsymbol{0} \\ \boldsymbol{L}_4\boldsymbol{B}_w & -\boldsymbol{L}_3\end{bmatrix}\begin{bmatrix}\boldsymbol{w}_j \\ \dot{\boldsymbol{w}}_j\end{bmatrix}\right) \tag{11}$$

where

$$\boldsymbol{L}_3 = (\boldsymbol{A}_{bw0}\boldsymbol{W}_4^{-1}\boldsymbol{W}_3 - \boldsymbol{A}_{bb})^{-1}, \boldsymbol{L}_4 = \boldsymbol{L}_3\boldsymbol{A}_{bw1} \tag{12}$$

Equations (8) and (11) constitute the state-space formulation of the UVLM as follows:

$$\begin{cases} \dot{\boldsymbol{\Gamma}}_{w1} = \boldsymbol{A}_a\boldsymbol{\Gamma}_{w1} + \boldsymbol{B}_a\begin{bmatrix}\boldsymbol{w}_j \\ \dot{\boldsymbol{w}}_j\end{bmatrix} \\ \boldsymbol{F}_a = \boldsymbol{C}_a\boldsymbol{\Gamma}_{w1} + \boldsymbol{D}_a\begin{bmatrix}\boldsymbol{w}_j \\ \dot{\boldsymbol{w}}_j\end{bmatrix} \end{cases} \tag{13}$$

In the aforementioned UVLM-based state-space model for unsteady aerodynamics, the state variables correspond to the wake vortex strengths from the second row onward, while the input variables are the downwash velocity on the wing surface and its rate of change.

### *2.3. Propeller Numerical Modeling: Slipstream Tube Model*

In Equation (13), the input variables are the downwash velocity on the wing surface and its rate of change. The wing downwash includes contributions from structural vibrations, freestream velocity, and propeller slipstream, with the downwash induced by the propeller slipstream being an important component in the aerodynamic modeling of the

DEP system. To evaluate this downwash, the STM proposed by Nederlof [53] et al. is employed in this study.

When the propeller blades rotate, helicoidal wake vortices are generated, and additionally the bound vortices on the blades also affect the flow field. Together, these two components determine the induced velocity distribution within the propeller slipstream. At a given point in the slipstream, the magnitude of the induced velocity depends on the relative position of the blades and the spatial orientation of the vortices, meaning that the blade azimuth and the helicoidal distribution of the vortices influence the local velocity. However, if only the time-averaged effects are of interest, it is unnecessary to model such complex transient vortex structures. Therefore, under the time-averaged framework, the instantaneous discrete blade azimuth angle is essentially averaged out, which means that the specific phase synchronization among distributed propellers (such as randomized azimuth angles) does not need to be explicitly parameterized. A simpler model can be employed to represent the main characteristics of the slipstream. This simplified approach is the STM, in which the complex helicoidal vortices are simplified into axial and tangential vorticity components that are shed continuously from the propeller disc along the radial direction. This approach transforms the discrete blade-vortex structures into a continuously distributed vortex system, thereby representing the characteristics of the slipstream. Figure 9 illustrates the schematic of the STM.

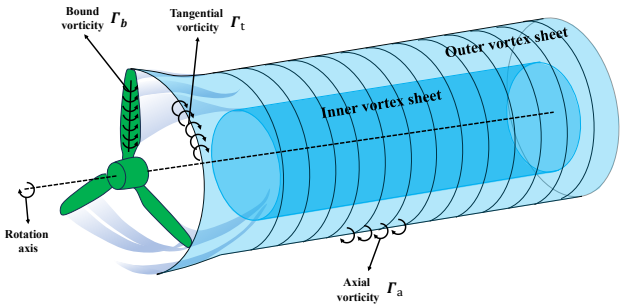



**Figure 9.** Schematic diagram of the STM.

The STM is a rapid and low-cost method for quantitatively estimating the induced velocities inside the slipstream. Its fundamental calculation still relies on the Biot–Savart law, where the induced velocities corresponding to the three types of vorticity distributions are computed separately and then superimposed to obtain the propeller slipstream induced velocity. Figure 10 illustrates the schematic of the induced velocity contributions generated by the three vorticity components at a spatial point $P$.

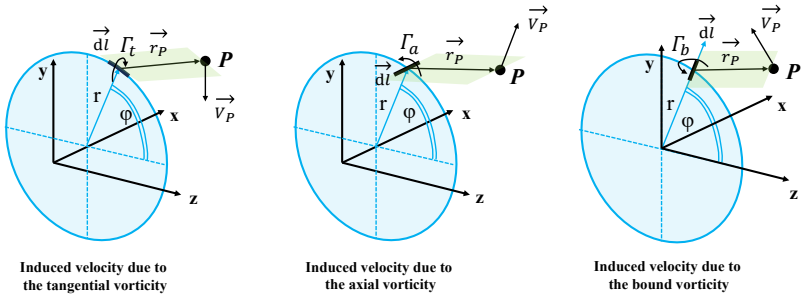



**Figure 10.** The induced velocity contributions of the three different vorticity components at a spatial point $P$.

Based on the derivation presented in Reference [53], the induced velocity formulas for the three different vorticity components are directly given.

**a. Tangential vorticity**

The tangential vorticity is the primary contributor to the axial induced velocity in the propeller slipstream. The induced velocity components in the $x$, $y$, and $z$ directions can be calculated using the following formulas.

$$V_{P,x} = \sum_{i=1}^{N} \frac{nB}{4\pi V_\infty} \frac{(1-a_i')}{(1+a_i)} \left(\frac{\Delta\Gamma_p}{\Delta r}\right)_i r_i \sum_{j=1}^{M} \frac{c_{i,j}\cos(j\Delta\varphi) + b_{i,j}\sin(j\Delta\varphi)}{l_{i,j}^2} \left(1 + \frac{x_P}{\sqrt{x_P^2 + l_{i,j}^2}}\right) \Delta\varphi\Delta r \tag{14}$$

$$V_{P,y} = \sum_{i=1}^{N} \frac{nB}{4\pi V_\infty} \frac{(1-a_i')}{(1+a_i)} \left(\frac{\Delta\Gamma_p}{\Delta r}\right)_i r_i \sum_{j=1}^{M} \frac{\sin(j\Delta\varphi)}{\sqrt{x_P^2 + l_{i,j}^2}} \Delta\varphi\Delta r \tag{15}$$

$$V_{P,z} = \sum_{i=1}^{N} \frac{nB}{4\pi V_\infty} \frac{(1-a_i')}{(1+a_i)} \left(\frac{\Delta\Gamma_p}{\Delta r}\right)_i r_i \sum_{j=1}^{M} \frac{\cos(j\Delta\varphi)}{\sqrt{x_P^2 + l_{i,j}^2}} \Delta\varphi\Delta r \tag{16}$$

$$\begin{aligned} &b_{i,j} = y_P - r_i\sin(j\Delta\varphi), c_{i,j} = z_P - r_i\cos(j\Delta\varphi) \\ &l_{i,j}^2 = b_{i,j}^2 + c_{i,j}^2 \end{aligned} \tag{17}$$

In the above equations, $N$ denotes the number of radial discretization segments of the propeller blades, and $M$ represents the number of azimuthal discretization segments on the propeller disk plane. The variable $n$ denotes the propeller rotational speed, $B$ is the number of propeller blades, $r$ is the radial position coordinate of the propeller, $\varphi$ is the azimuthal angle on the propeller disk, and $\Gamma_p$ represents the circulation of each discretized radial segment of the propeller. The parameters $a$ and $a'$ correspond to the axial and tangential induction factors, respectively, while $x_P$, $y_P$, and $z_P$ denote the coordinates of a spatial point $P$. The parameters $b_{i,j}$ and $c_{i,j}$ represent the relative distances in the $y$ and $z$ directions, respectively, between the evaluation point $P(x_P, y_P, z_P)$ and the $j$-th azimuthal discrete element located at the $i$-th radial station on the propeller disk. Once the radial discretization number $N$ and the azimuthal discretization number $M$ are specified, $r$ and $\varphi$ are determined. However, $\Gamma_p$, $a$, and $a'$ must be calculated using the blade element momentum (BEM) theory.

The BEM model [54,55] is a commonly used tool for analyzing propeller performance, as it can provide accurate and efficient results based on the geometric characteristics of the propeller blades. The circulation $\Gamma_p$ at each radial segment can be calculated using the following expression:

$$\begin{aligned} \Gamma_p(r) &= \frac{V_{eff} c C_l}{2} \\ V_{eff} &= \sqrt{(V_\infty(1+a))^2 + (\omega r(1-a'))^2} \end{aligned} \tag{18}$$

The local chord length $c$ is determined from the propeller geometric parameters, while the local lift coefficient $C_l$ is obtained from airfoil aerodynamic data using a lookup table. The angular velocity $\omega$ is derived from the rotational speed. Figure 11 illustrates the geometric parameters of the propeller airfoil sections. The determination of $a$ and $a'$ requires explicit iteration based on the propeller geometry. Figure 12 presents the explicit iterative procedure for solving $a$ and $a'$.

**b. Axial vorticity**

In propeller slipstream modeling, the axial vorticity primarily determines the swirl velocity component within the slipstream. Its distribution is idealized as straight vortex lines aligned with the axis of rotation, extending semi-infinitely downstream at different radial and azimuthal positions, thereby forming cylindrical surfaces in the circumferential

direction. The induced velocity due to the axial vorticity can be calculated using the following expression:

$$V_{P,x} = 0 \tag{19}$$

$$V_{P,y} = \sum_{i=1}^{N} \frac{B}{8\pi^2} \left( \frac{\Delta \Gamma_p}{\Delta r} \right)_i \sum_{j=1}^{M} \frac{c_{i,j}}{l_{i,j}^2} \left( 1 + \frac{x_P}{\sqrt{x_P^2 + l_{i,j}^2}} \right) \Delta\varphi \Delta r \tag{20}$$

$$V_{P,z} = \sum_{i=1}^{N} \frac{B}{8\pi^2} \left( \frac{\Delta \Gamma_p}{\Delta r} \right)_i \sum_{j=1}^{M} \frac{-b_{i,j}}{l_{i,j}^2} \left( 1 + \frac{x_P}{\sqrt{x_P^2 + l_{i,j}^2}} \right) \Delta\varphi \Delta r \tag{21}$$

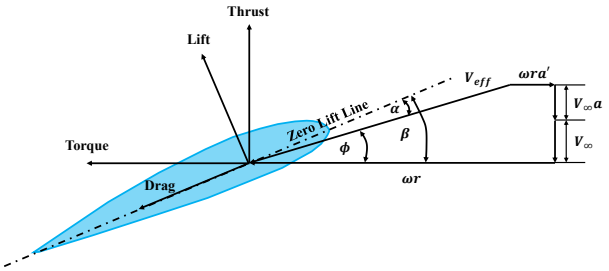



**Figure 11.** Schematic diagram of the geometric parameters of the propeller airfoil section.

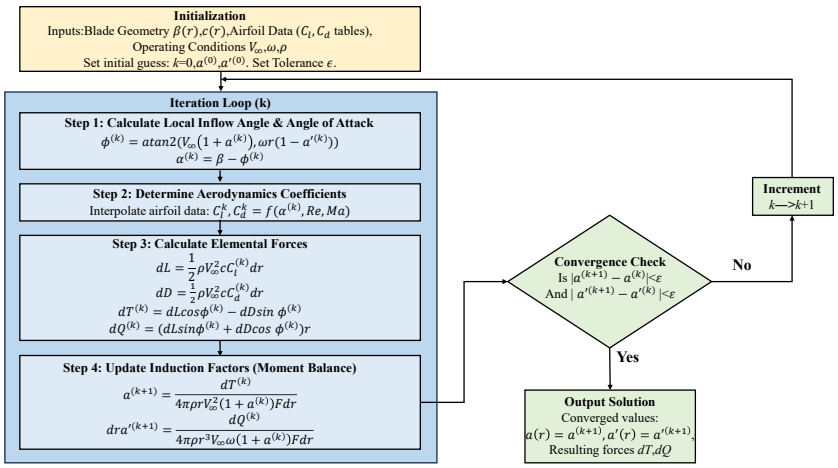



**Figure 12.** The explicit iteration procedure for solving $a$ and $a'$.

### c. Bound vorticity

To accurately capture the tangential flow features (swirl) in the immediate vicinity of the rotor plane, the contribution of the propeller's bound circulation must be explicitly included. These bound vortices are idealized as a series of concentric rings located at the disk station. While their induced effect attenuates rapidly along the streamwise direction, they are indispensable for maintaining the correct velocity boundary conditions near the blades. Consequently, the induced velocity component derived from the bound vorticity is evaluated as follows:

$$V_{P,x} = \sum_{i=1}^{N} \left( \frac{B\Gamma_p}{8\pi^2} \right)_i \sum_{j=1}^{M} \frac{-y_P \cos(j\Delta\varphi) + z_P \sin(j\Delta\varphi)}{(x_P^2 + l_{i,j}^2)^{3/2}} \Delta\varphi \Delta r \tag{22}$$

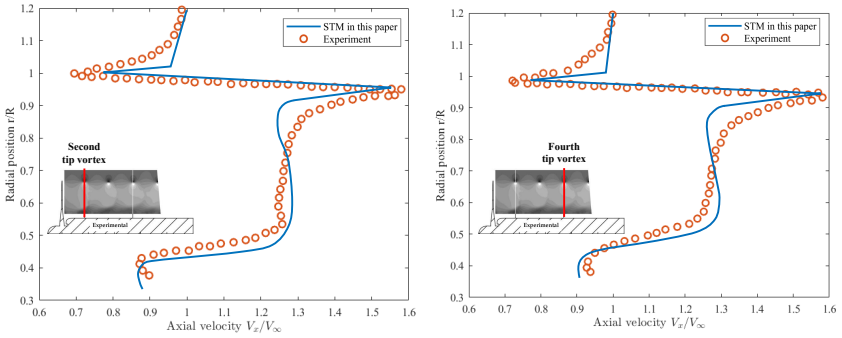
$$V_{P,y} = \sum_{i=1}^{N} \left( \frac{B\Gamma_p}{8\pi^2} \right)_i \sum_{j=1}^{M} \frac{x_P \cos(j\Delta\varphi)}{(x_P^2 + l_{i,j}^2)^{3/2}} \Delta\varphi \Delta r \tag{23}$$

$$V_{P,z} = \sum_{i=1}^{N} \left( \frac{B\Gamma_p}{8\pi^2} \right)_i \sum_{j=1}^{M} \frac{-x_P \sin(j\Delta\varphi)}{\left(x_P^2 + l_{i,j}^2\right)^{3/2}} \Delta\varphi \Delta r \tag{24}$$

The induced velocity at a spatial point $P$ within the propeller slipstream is obtained by superposing the three types of vortices. However, due to the singularity present in inviscid vortex methods near the vortex filament core, the evaluation point should not coincide with the vortex filaments. To reduce discretization errors and introduce a certain degree of viscous effects, the vortex-core model described in Equation (2) can be applied.

To verify the accuracy and reliability of the STM method in this study, the Beaver propellers reported by Alvarez [56] et al. and Stokkermans [57] et al. were used as examples. The free-stream velocity was set to $V_\infty = 40$ m/s and the advance coefficient to $J = 0.8$. The geometric parameters of the Beaver propeller is shown in Figure 7.

Using the STM code developed in this study, the $x$-component of the induced velocity at the positions of the second and fourth tip vortices was calculated and compared with the experimental results reported by Stokkermans [57] et al. The comparison results are presented in Figure 13 and Table 3. As detailed in Table 3, the quantitative error analysis reveals that the mean relative errors for the second and fourth tip vortices are 10.19% and 8.71%, respectively. Although the inherent simplification assumptions of the STM introduce these moderate deviations, it can be observed that the overall induced velocity near the wingtip still agrees well with the experimental data. This acceptable error margin indicates that the proposed fast modeling approach successfully balances computational efficiency with the accuracy requirements of preliminary aerodynamic modeling.




(**a**) Second tip vortex (**b**) Fourth tip vortex

**Figure 13.** Comparison of axial induced velocity in the propeller wake.

**Table 3.** Error analysis between the STM and experimental measurements.

| Metric | Second Tip Vortex | Fourth Tip Vortex |
|---|---|---|
| RMSE | 0.1294 | 0.1113 |
| Max Absolute Error | 0.2737 | 0.2496 |
| Mean Relative Error (%) | 10.19 | 8.71 |

The induced velocity in the propeller slipstream region was calculated using the STM method and, based on Equation (13), incorporated as part of the wing downwash velocity. This induced velocity was then introduced into the UVLM aerodynamic state-space equations to compute the wing aerodynamic forces, thereby completing the aerodynamic modeling of the DEP system with consideration of propeller slipstream effects.

## 3. Structural Dynamics Modeling for DEP System

For the DEP system, as a core subsystem of a DEP aircraft, its structural dynamics not only influence the elastic deformation of the wing but also have an impact on the wing's aerodynamic characteristics. Therefore, conducting the structural dynamics model of this system carries profound and complex physical significance. The core challenge lies in the introduction of the strongly coupled "aero-propulsive-elastic" effects arising from the deep integration of the propulsion system and the wing. Unlike a conventional wing, the multiple distributed electric propulsion units along the wing span generate slipstreams that alter the local flow field over specific wing regions, inducing variations in local dynamic pressure and effective angle of attack. This characteristic introduces a novel coupling pathway, which is where the elastic deformation of the wing (such as bending and torsion) modifies its relative attitude within the propeller slipstream, thereby instantaneously altering the additional aerodynamic forces generated by slipstream-induced lift enhancement. These aerodynamic load variations, in turn, react on the wing structure, affecting its deformation and vibration and thereby establishing a rapid closed-loop feedback mechanism: structural deformation → change in local aerodynamic characteristics → modification of the propulsion system's slipstream effect → shift in aerodynamic forces → structural dynamic response.

In this section, a linear elastic finite element analysis method is employed, and the mass distribution is simplified using a lumped mass approach.

### *3.1. Structural Dynamic Equations*

The wing structure of the DEP system is discretized into an $n$-node finite element model. In physical coordinates, the governing equation of structural dynamics is expressed as:

$$\boldsymbol{M}\ddot{\boldsymbol{u}}(t) + \boldsymbol{C}\dot{\boldsymbol{u}}(t) + \boldsymbol{K}\boldsymbol{u}(t) = \boldsymbol{f}_{ext}(t) \tag{25}$$

where $\boldsymbol{M}$, $\boldsymbol{C}$, and $\boldsymbol{K}$ denote the mass, structural damping, and stiffness matrices, respectively. The vector $\boldsymbol{u}(t)$ represents the physical nodal displacements, while $\boldsymbol{f}_{ext}$ encompasses gravity, aerodynamic forces, propeller thrust, and coriolis moment of the propeller, where gravity is assumed to be constant, and the calculation of aerodynamic forces and propeller thrust is based on the theoretical model in Section 2. Thus, this equation forms the structural aerodynamic–propulsion coupled model.

To enhance computational efficiency, modal superposition is applied via the transformation $\boldsymbol{u} = \boldsymbol{\Phi}\boldsymbol{\eta}$, where $\boldsymbol{\Phi}$ is the modal matrix and $\boldsymbol{\eta}$ represents the modal coordinates. Substituting this transformation into Equation (25) and pre-multiplying by $\boldsymbol{\Phi}^T$ yields the structural dynamic equation in modal space:

$$\boldsymbol{\Phi}^T\boldsymbol{M}\boldsymbol{\Phi}\ddot{\boldsymbol{\eta}} + \boldsymbol{\Phi}^T\boldsymbol{C}\boldsymbol{\Phi}\dot{\boldsymbol{\eta}} + \boldsymbol{\Phi}^T\boldsymbol{K}\boldsymbol{\Phi}\boldsymbol{\eta} = \boldsymbol{\Phi}^T\boldsymbol{f}_{ext} \tag{26}$$

From Equation (26), it can be observed that the modal matrix $\boldsymbol{\Phi}$, the mass matrix $\boldsymbol{M}$, and the stiffness matrix $\boldsymbol{K}$ are the fundamental parameter matrices for constructing the structural dynamics model. The wing geometric parameters of the system analyzed herein are presented in Table 4. Modal analysis is performed using a finite element numerical code. The obtained modal shapes and frequencies are shown in Figure 14 and Table 5. As shown in Table 5, the finite element modal frequencies obtained in the present study are in good agreement with the experimental results [39].

**Table 4.** Fundamental parameters of the DEP system.

| Parameter | Value |
|---|---|
| Aspect ratio | 15 |
| Mean aerodynamic chord (m) | 0.65 |
| Wing span (m) | 9.63 |
| Wing area ($m^2$) | 6.22 |
| Taper ratio | 0.7 |
| Tip chord (m) | 0.53 |
| Root chord (m) | 0.76 |
| Wing weight (kg) | 141.9 |
| DEP module weight (kg) | $6.8 \times 12$ |

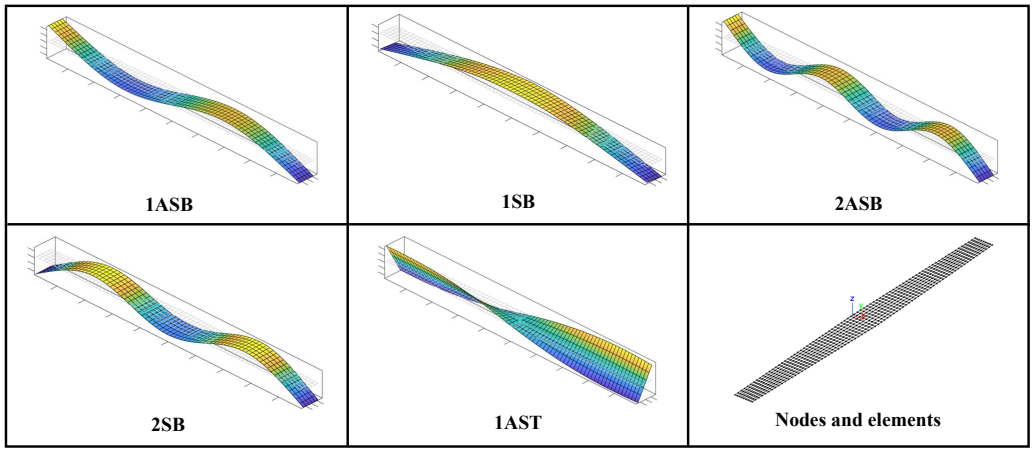



**Figure 14.** The modal shapes, as well as the finite elements and nodes of the wing (AS: Antisymmetric, S: Symmetric, B: Bending, T: Torsion).

**Table 5.** Comparison between numerical and experimental modal frequencies.

| Mode | 1 | 2 | 3 | 4 | 5 |
|---|---|---|---|---|---|
| Finite element analysis (Hz) | 2.18 | 2.62 | 15.09 | 15.52 | 23.68 |
| Experimental Testing (Hz) | 2.14 | 2.56 | 14.82 | 15.76 | 22.81 |
| Relative error (%) | 1.87 | 2.34 | 1.82 | 1.52 | 3.81 |

### *3.2. Displacement Interpolation and Equivalent Aerodynamic Force*

To facilitate data exchange between the finite element nodes and the aerodynamic grid (Figure 15), the infinite plate spline method [42] is employed. This approach, based on the small-deflection theory of an infinite plate, relates the transverse displacement $w(x, y)$ at any point $(x, y)$ to a set of loads applied at $N_s$ structural nodes:

$$w(x, y) = a_0 + a_1 x + a_2 y + \sum_{i=1}^{N_s} F_i r_i^2 \ln r_i^2 \tag{27}$$

where $r_i^2 = (x - x_i)^2 + (y - y_i)^2$ is the Euclidean distance to the $i$-th structural node. To ensure equilibrium at infinity, the constraints $\sum F_i = \sum x_i F_i = \sum y_i F_i = 0$ are imposed.

For the set of $N_s$ structural nodes, the displacement vector $\boldsymbol{u}_s$ and the interpolation coefficients are related by the following linear system:

$$\begin{bmatrix} \mathbf{0} \\ \boldsymbol{u}_s \end{bmatrix} = \underbrace{\begin{bmatrix} \mathbf{0} & \boldsymbol{R}_s^T \\ \boldsymbol{R}_s & \boldsymbol{K}_s \end{bmatrix}}_{\boldsymbol{C}_s} \begin{bmatrix} \boldsymbol{a} \\ \boldsymbol{F} \end{bmatrix} \tag{28}$$

where $\boldsymbol{a} = [a_0, a_1, a_2]^T$ and $\boldsymbol{F}$ is the vector of nodal loads. $\boldsymbol{R}_s$ is the coordinate matrix with rows $[1, x_i, y_i]$, and the kernel matrix $\boldsymbol{K}_s$ is defined by elements $K_{ij} = r_{ij}^2 \ln r_{ij}^2$ (with $K_{ii} = 0$).

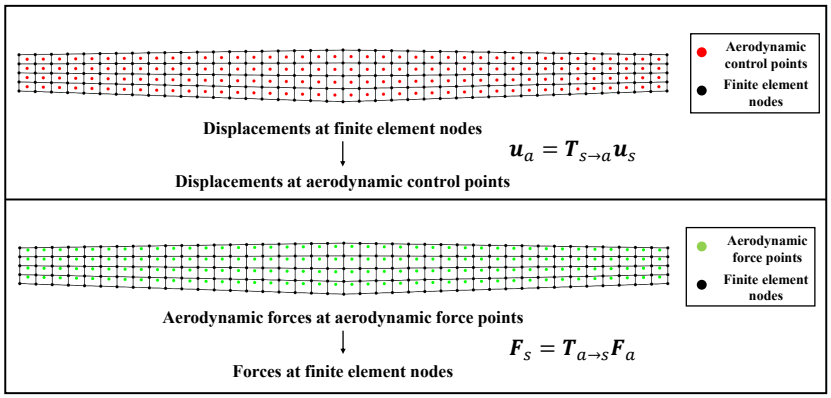



**Figure 15.** Schematic of deformation displacement and aerodynamic force interpolation.

Similarly, the displacements at $N_a$ aerodynamic control points, $\boldsymbol{u}_a$, are interpolated via:

$$\boldsymbol{u}_a = \underbrace{\begin{bmatrix} \boldsymbol{R}_a & \boldsymbol{K}_a \end{bmatrix}}_{\boldsymbol{C}_a} \begin{bmatrix} \boldsymbol{a} \\ \boldsymbol{F} \end{bmatrix} \tag{29}$$

where the definitions of $\boldsymbol{R}_a$ and $\boldsymbol{K}_a$ are analogous to those of $\boldsymbol{R}_s$ and $\boldsymbol{K}_s$, utilizing the coordinate information of the aerodynamic grid points.

By combining Equations (28) and (29), the displacement transfer relationship is established:

$$\boldsymbol{u}_a = \boldsymbol{C}_a \boldsymbol{C}_s^{-1} \begin{bmatrix} \mathbf{0} \\ \boldsymbol{u}_s \end{bmatrix} = \boldsymbol{T}_{s\to a} \boldsymbol{u}_s \tag{30}$$

According to the principle of virtual work ($\Delta \boldsymbol{u}_a^T \boldsymbol{F}_a = \Delta \boldsymbol{u}_s^T \boldsymbol{F}_s$), the equivalent aerodynamic forces $\boldsymbol{F}_a$ are transferred back to the structural nodes using the transpose of the interpolation matrix:

$$\boldsymbol{F}_s = \boldsymbol{T}_{s\to a}^T \boldsymbol{F}_a \tag{31}$$

where $\boldsymbol{T}_{a\to s} = \boldsymbol{T}_{s\to a}^T$ represents the force transfer matrix from the aerodynamic grid to the structural nodes.

## 4. Integration of Flexible DEP System Model

After establishing the models of each subsystem of the DEP system, the integrated aeroelastic model of the full system is constructed based on the input–output relationships among the subsystem models, as illustrated in Figure 16. The inputs of the full system model include throttle commands and freestream velocity. Throttle commands are converted into propeller thrust via propeller dynamics and coupled with the wing structure through interpolation. The UVLM aerodynamic model is linearized into the state-space form. The inputs of the aerodynamic state-space model consist of downwash and downwash rate, while the outputs are aerodynamic forces and moments. The downwash comprises three components: freestream velocity downwash, slipstream induced

downwash, and wing deformation induced downwash. Accordingly, the downwash is calculated as follows:

$$\boldsymbol{w}_j = \boldsymbol{M}_{fv}\boldsymbol{V}_\infty + \boldsymbol{w}_{prop} + (\boldsymbol{D}_{1jk}\boldsymbol{T}_{s\to a}\boldsymbol{u}_s + \boldsymbol{D}_{2jk}\boldsymbol{T}_{s\to a}\dot{\boldsymbol{u}}_s) \tag{32}$$

where $\boldsymbol{M}_{fv}$ is the coefficient matrix that transforms the freestream velocity $\boldsymbol{V}_\infty = [u, v, w]^T$ into the downwash, $\boldsymbol{w}_{prop}$ denotes the slipstream-induced downwash obtained through the STM method, $\boldsymbol{D}_{1jk}$ and $\boldsymbol{D}_{2jk}$ are the differentiation matrices that define the kinematic boundary conditions on the lifting surface. Specifically, $\boldsymbol{D}_{1jk}$ accounts for the change in the local incidence angle (slope) due to the structural deformation, while $\boldsymbol{D}_{2jk}$ relates the translational velocity of the aerodynamic panels to the induced downwash. These matrices effectively map the motion of the aerodynamic grid points, interpolated from the structural grid via $\boldsymbol{T}_{s\to a}$, to the corresponding normal wash at the collocation points.

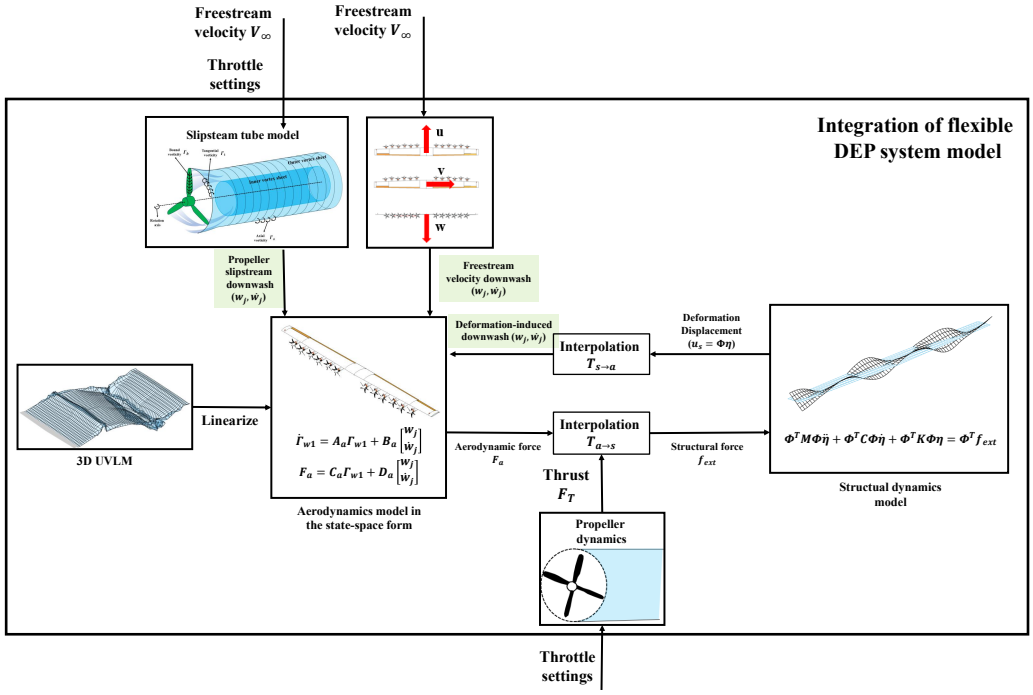



**Figure 16.** Framework of the aeroelastic model for the DEP system.

By differentiating Equation (32) with respect to time, the downwash rate $\dot{\boldsymbol{w}}_j$ can be directly obtained. The downwash and its rate are used as inputs to the aerodynamic state-space model, when combined with the current freestream velocity, yields the aerodynamic loads $\boldsymbol{F}_a$ at the aerodynamic load points. The aerodynamic loads, together with the distributed propeller thrusts and coriolis moments, are mapped to the finite element nodes through the interpolation matrix $\boldsymbol{T}_{a\to s}$, serving as the resultant external loads of the DEP system. Based on the external loads, the structural dynamic equations can be solved to obtain the wing deformation $[\boldsymbol{\eta}, \dot{\boldsymbol{\eta}}]^T$. Subsequently, the interpolation matrix $\boldsymbol{T}_{s\to a}$ is used to convert the wing deformation into the deformation-induced downwash and its rate, while the coefficient matrix $\boldsymbol{M}_{fv}$ transforms the freestream velocity into the freestream-induced downwash and its rate. Through the above process, a coupled modeling framework is established both the aerodynamics and structural dynamics.

## 5. Numerical Results

The preceding sections have provided a detailed introduction to the theory and implementation of constructing an aeroelastic model of the DEP system by integrating the

UVLM and STM methods, and the individual subsystems have been validated. In this section, the aeroelastic model of the DEP system is derived. The objectives of this study are twofold: first, to capture the aero-structural coupling effects between the distributed propeller slipstreams and the flexible main wing; second, to investigate the effect of the reaction torque of the distributed propellers on the aeroelastic response of the wing.

As shown in Figure 1, the DEP system is equipped with twelve high-lift propellers that are uniformly distributed along the wingspan. According to the blade element theory [55], the thrust of the high-lift propellers can be expressed as follows:

$$dT = B \cdot \frac{1}{2}\rho V_{res}^2 c(C_l \cos\phi - C_d \sin\phi)dr \tag{33}$$

$$dQ = B \cdot \frac{1}{2}\rho V_{res}^2 c(C_l \sin\phi + C_d \cos\phi)rdr \tag{34}$$

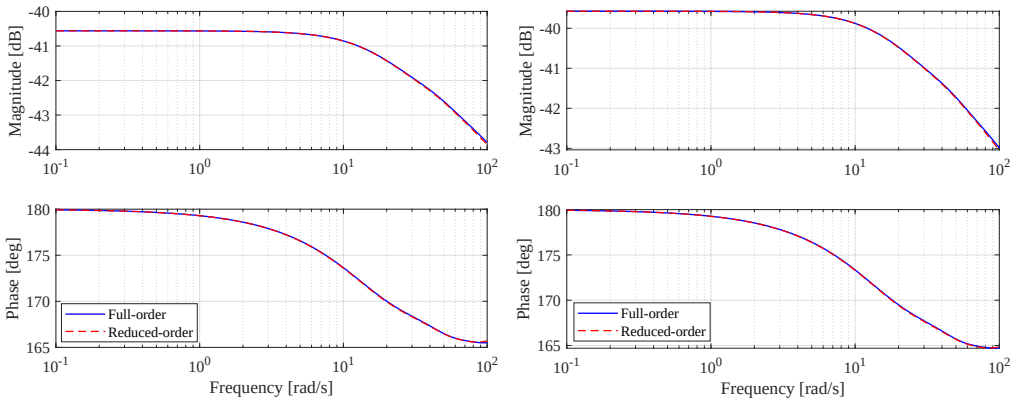
where $B$ denotes the number of blades, $c$ is the sectional chord length, and $V_{res}$ represents the resultant velocity, which accounts for the freestream velocity, rotational velocity, and slipstream-induced velocity. $C_l$ and $C_d$ are the sectional lift and drag coefficients, respectively, and $\phi$ signifies the inflow angle.

### *5.1. Aerodynamic Modeling*

The aerodynamic model of the DEP system is established based on the UVLM, including the discretization of the boundary grid and the generation of initial trailing vortices. The model comprises 320 boundary panels to ensure that the elemental forces accurately capture the spanwise and chordwise distribution of lift. The number of trailing vortices is determined to be 2760 through a convergence analysis, corresponding to an aerodynamic state-space model with 2720 states.

To maintain computational tractability for the subsequent aeroelastic coupling and stability analysis, model order reduction is performed on the high-dimensional aerodynamic system. The original UVLM-based state-space model, containing 2720 states, is inherently sparse but computationally burdensome for integrated simulations. In this study, the balanced truncation method [58] is employed, which identifies a realization where the states are equally controllable and observable. By solving the dual Lyapunov equations for the controllability and observability Gramians, the hankel singular values are calculated to quantify the energy contribution of each state to the input–output behavior. The system's dynamics are dominated by a small subset of energy-rich states, allowing the model to be truncated to 45 states while retaining the core unsteady aerodynamic characteristics.

The significance of employing Bode plots for verification lies in the frequency-dependent nature of unsteady aerodynamics. For aeroelastic, the phase lag and magnitude attenuation of the aerodynamic loads relative to the structural motion (downwash) are important. Therefore, the Bode plots in Figure 17 are utilized to evaluate whether the reduced-order model preserves the transfer function characteristics of the full-order model across the frequency range of interest. The degree of overlap in the frequency response curves ensures that the reduced-order model captures the circulatory and non-circulatory lift effects. This validated low-order model is then integrated with the propeller slipstream module, where the slipstream-induced downwash is treated as a specialized input for aerodynamic grid points within the propeller wake.




(**a**) $w_j$ to the resultant force $F_z$ (**b**) $w_j$ to the resultant moment $M_x$

**Figure 17.** Comparison of the unsteady aerodynamic force/moment before and after balanced truncation.

### *5.2. Flexible Structure Modeling and Interpolation*

A six-degree-of-freedom four-node shell element is selected for the finite element structural modeling. The finite element results have been presented in Section 3.1 (see Figure 14). In this study, the wing is discretized into 375 finite elements, comprising 456 nodes and 2736 degrees of freedom. The first six modes are selected to construct the modal matrix.

Considering that the finite element mesh does not coincide with the aerodynamic grid, the finite element nodes, aerodynamic grid control points, and aerodynamic load points are chosen as interpolation points to construct the interpolation matrices $\boldsymbol{T}_{s\to a}$ and $\boldsymbol{T}_{a\to s}$.

### *5.3. Nonlinear Simulations*

To demonstrate the nonlinear numerical results, a throttle input disturbance is applied to the system. Six disturbance cases are considered: one-engine disturbance, two-engine disturbance, three-engine disturbance, four-engine disturbance, five-engine disturbance, and six-engine disturbance. The freestream velocity is set to $V_\infty = 36, 40, 50, 66$ m/s. A schematic illustration of these cases is shown in Figure 18. The throttle disturbance is implemented as a sinusoidal excitation with an angular frequency of $4\pi$ rad/s. The signal oscillates during the initial interval $t \in [0, 4]$ s and is specifically designed to reach zero at $t = 4$ s to ensure a smooth transition. Subsequently, the disturbance is deactivated and remains at zero for the remainder of the simulation ($t \in [4, 6]$ s).

From the perspective of wing lift generation, Figure 19 illustrates the dynamic lift response of the wing at four different flight speeds ($V$ = 36, 40, 50, and 66 m/s) under six throttle disturbance conditions. The total lift increment is positively correlated with the number of motors introducing the disturbance. From the zoomed-in views at each speed, it can be observed that the system exhibits a stable forced oscillation response during the periodic throttle disturbance. As the asymmetric disturbances are sequentially accumulated from one to six engines, the peak amplitude of the lift oscillation exhibits a monotonic increase. Physically, this is because the involvement of more motors expands the spanwise region washed by the high dynamic pressure of the slipstream, enabling the superposition of the total circulation of the aircraft, which verifies the feasibility of the DEP system to achieve highly efficient lift enhancement through multi-engine distributed slipstreams. Furthermore, comparing the response curves across these four different speeds reveals the coupling characteristic that the slipstream aerodynamic control authority attenuates with speed. Under the low-speed condition of 36 m/s, the spacing between the disturbance branch curves is wide, and the slipstream disturbance occupies a larger aerodynamic weight; whereas under the high-speed condition of 66 m/s, the six curves are

compressed and closely aligned. This phenomenon indicates that during the low-speed phase, the slipstream velocity increment generated by the motors accounts for a larger proportion of the total flow field, and the DEP system exhibits high active aerodynamic control authority. Conversely, during the high-speed phase, the freestream dominates the dynamic pressure, thereby weakening the relative influence of the throttle disturbance. This phenomenon theoretically supports the operational concept of DEP aircraft, namely: the distributed slipstream is an excellent mechanism for achieving high lift during the low-speed flight phase (such as short takeoff and landing), whereas its relative aerodynamic weight decreases during the high-speed cruise phase.

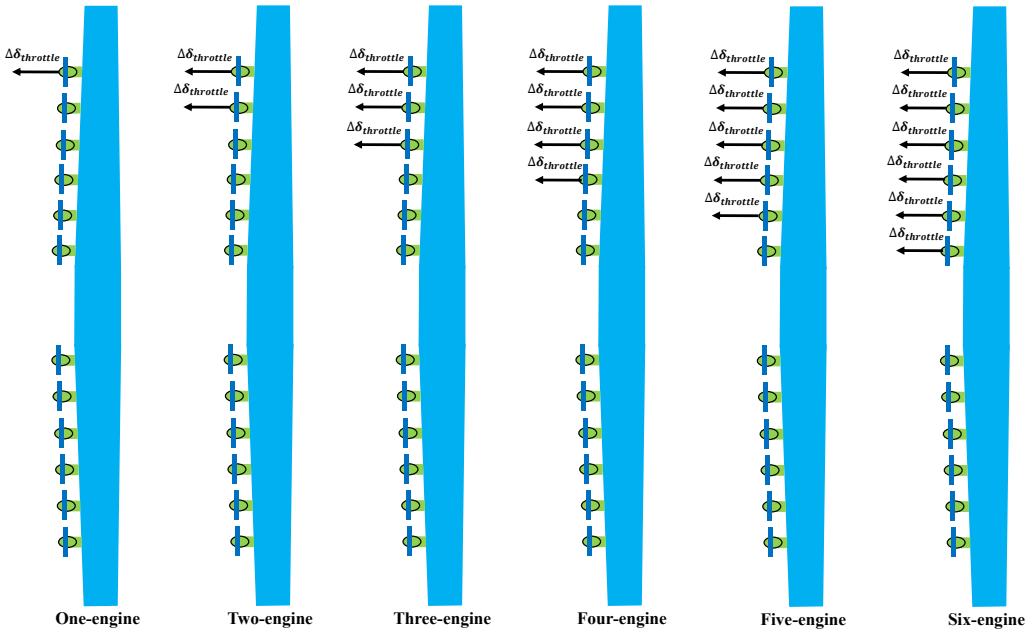
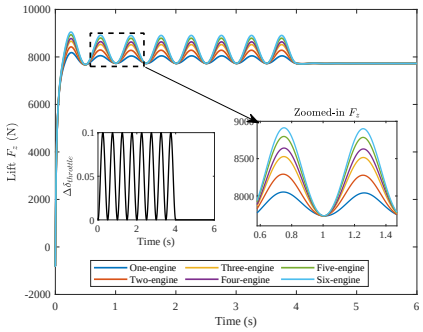


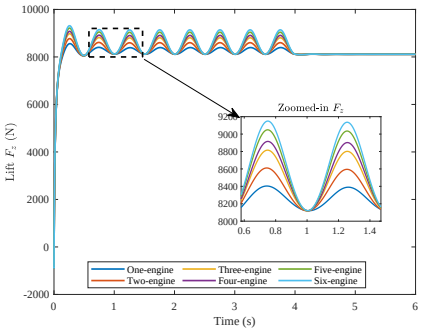

**Figure 18.** Schematic diagram of throttle input disturbances.

From the perspective of spanwise aerodynamic loading, Figure 20 illustrates the spanwise sectional lift coefficient ($c_l$) distribution of the wing under six asymmetric throttle disturbance conditions at four different flight speeds at $t$ = 1 s. The full wingspan exhibits 12 lift peaks corresponding to the 12 leading-edge high-lift propellers. Under all asymmetric disturbance conditions, the curves on the right half-wing ($2y/b > 0$) are highly coincidental, serving as the undisturbed baseline reference; whereas on the left half-wing ($-1 < 2y/b < 0$), as the throttle disturbances are sequentially activated from the outermost location toward the wing root (from one to six engines), the corresponding local lift peaks emerge successively. This demonstrates the direct enhancement effect of the local high dynamic pressure induced by the propeller slipstream on the lift of the downstream wing sections. Observing the left half-wing, it can be found that when the disturbance conditions accumulate from one to five engines, the amplitudes of the already activated outboard peaks remain largely independent and stable. However, when the innermost sixth engine is activated (Six-engine, light blue curve), it not only generates a new peak at the wing root but also induces a secondary elevation across all previously activated lift peaks in the regions of engines 1 to 5. Comparing the subfigures across the four different speeds, it can be seen that as the freestream velocity increases from 36 m/s to 66 m/s, the relative prominence of the lift peaks compared to the non-slipstream valleys gradually diminishes (the maximum peak value on the left wing converges from approximately 3.3 to around 2.8). The underlying physical mechanism is that, at higher flight speeds, the freestream dynamic pressure dominates the flow field over the wing surface, and the proportion of

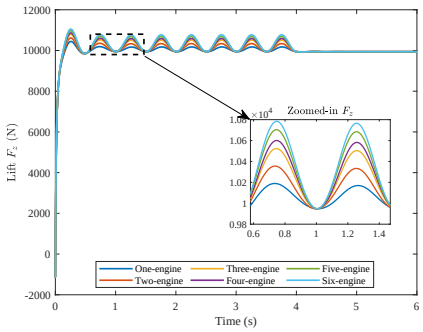
the slipstream velocity increment excited by the motor throttle disturbance within the local total dynamic pressure decreases.



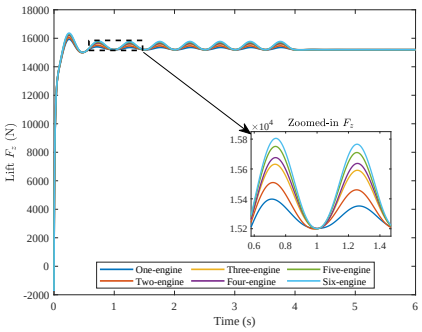

(**a**) $V$ = 36 m/s




(**b**) $V$ = 40 m/s

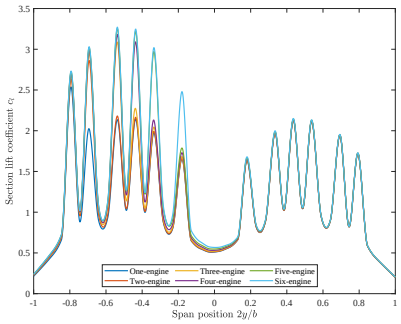



(**c**) $V$ = 50 m/s

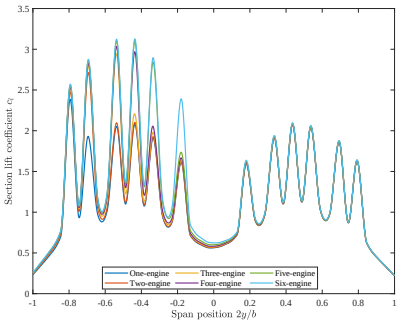



(**d**) $V$ = 66 m/s

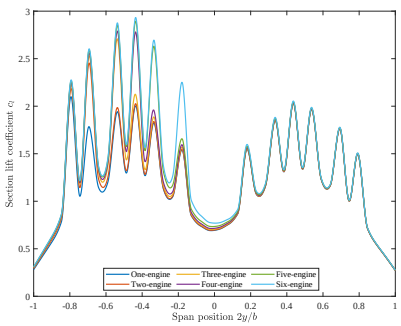
**Figure 19.** The dynamic lift response of the wing.



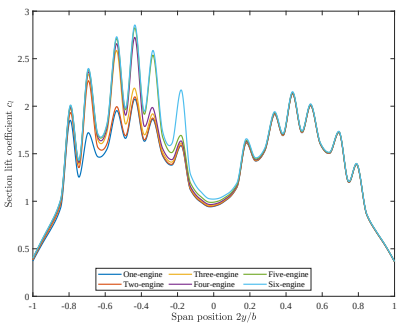

(**a**) $V$ = 36 m/s




(**b**) $V$ = 40 m/s




(**c**) $V$ = 50 m/s

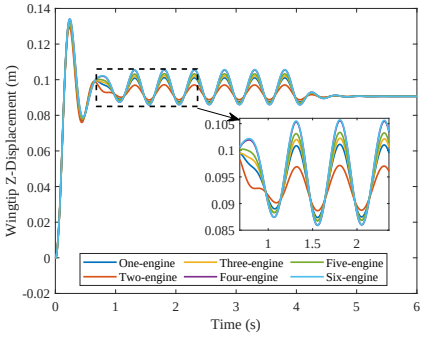



(**d**) $V$ = 66 m/s

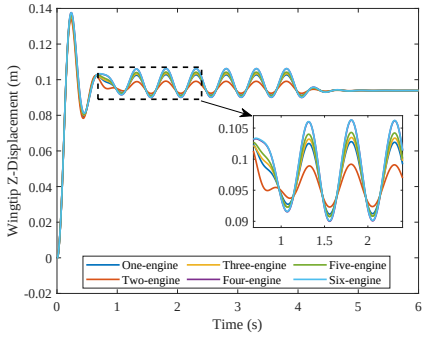
**Figure 20.** The spanwise sectional lift coefficient ($c_l$) distribution of the wing.

To analyze the wing deformation under different throttle disturbances, the displacements of the wingtip were extracted. Figure 21 illustrates the vertical displacement response of the wingtip under six asymmetric throttle disturbance conditions at various flight speeds. This set of curves verifies a core mechanism of the present study: in a DEP system, altering the throttle settings of local motors can actively reconfigure the aerodynamic load distribution on the wing surface, thereby inducing and controlling the structural deformation of the wing. This is specifically manifested in the following two features. First, the motor throttle possesses a multi-dimensional deformation tailoring capability. Observing the zoomed-in plots at various speeds, it can be seen that switching among different asymmetric throttle configurations (from one to six engines) alters both the oscillation amplitude and the steady-state equilibrium point of the wingtip displacement. Notably, this throttle-induced deformation is not a linear superposition. This nonlinear characteristic demonstrates that the throttle of the DEP system can not only drive wing deformation but also achieve aeroelastic tailoring of the wing deformation state by combining motor commands at different locations. This provides direct physical evidence for utilizing high-bandwidth motors to replace traditional physical control surfaces for active flutter suppression or load alleviation. Second, the throttle-deformation control authority exhibits a speed-sensitive boundary. Under the low-speed condition of 36 m/s, the wingtip deformation trajectories induced by different throttle configurations present a broad separation band, indicating that the motor throttle possesses high control authority over the wing deformation at this stage. However, as the flight speed increases to 66 m/s, although the absolute deformation of the wing is globally elevated due to the increased freestream dynamic pressure, the relative deformation differences excited by throttle variations are compressed, causing the respective disturbance curves to converge. This indicates that the active control strategy utilizing the throttle to induce wing deformation is most efficient during the low-speed phase (e.g., short takeoff and landing, or low-speed gust encounters), whereas its control authority attenuates during the high-speed phase due to the dominance of the freestream. Figure 22 illustrates the dynamic evolution of the spanwise vertical displacement for the wing under six-engine throttle configurations at flight speed $V = 40$ m/s.

Consequently, the DEP system holds potential for active aeroelastic control: by precisely coordinating the throttle inputs of multiple distributed propellers, the system can act as an active vibration suppressor. This capability allows for the real-time mitigation of wing deformation and oscillatory behavior, not only ensuring structural integrity and aerodynamic stability but also providing a robust technical framework for future active load alleviation and weight-optimized wing designs in DEP aircraft.

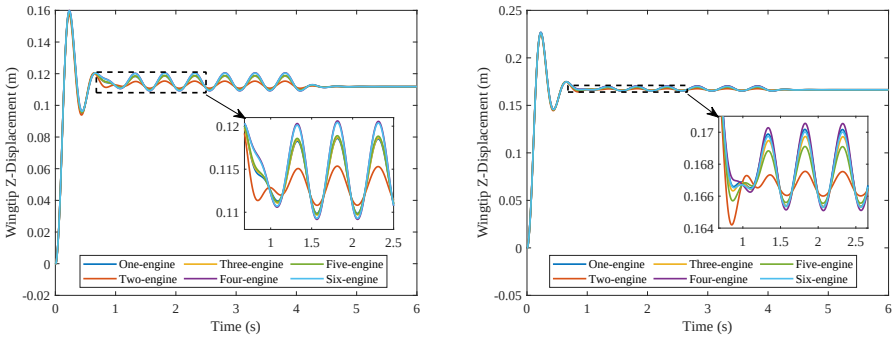



(**a**) $V = 36$ m/s




(**b**) $V = 40$ m/s

**Figure 21.** *Cont.*




(**c**) $V$ = 50 m/s (**d**) $V$ = 66 m/s

**Figure 21.** The vertical displacement response of the wingtip.

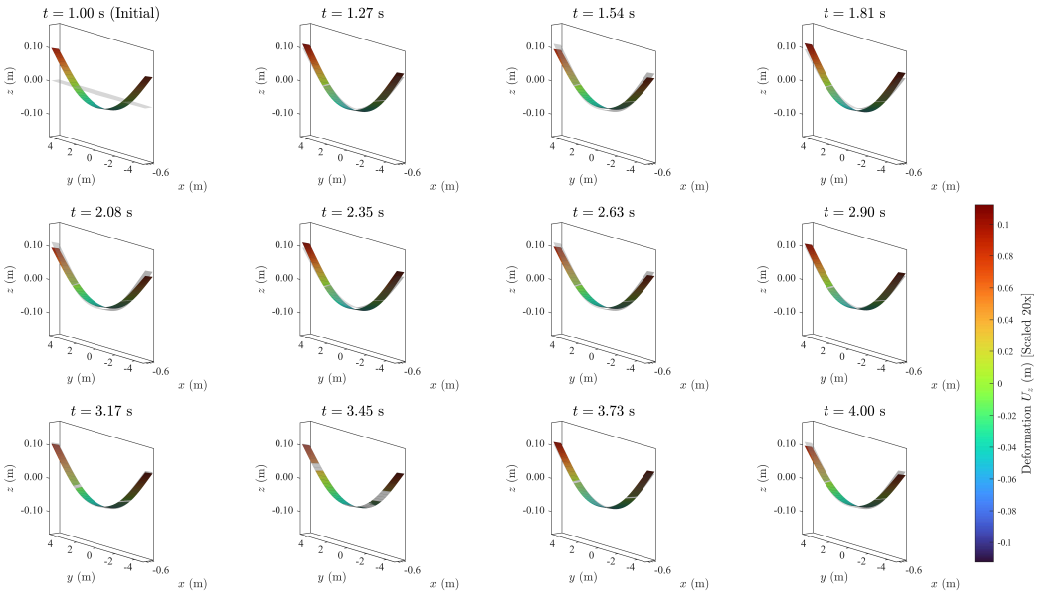



**Figure 22.** The dynamic evolution of the spanwise vertical displacement for the wing.

## 6. Conclusions

This paper develops an aeroelastic model for a DEP system that incorporates the effects of propeller slipstreams. The aerodynamic forces are modeled using the UVLM, and a state-space formulation is derived under the small-perturbation assumption, where the inputs are the downwash velocity and its rate of change, and the outputs are the aerodynamic forces and moments. The downwash of the DEP system primarily originates from three sources: freestream velocity, structural deformation, and propeller slipstream induction. The slipstream-induced downwash is computed using a slipstream tube model, which offers high computational efficiency and moderate accuracy.

Based on the coupling relationships among the subsystems, a complete aeroelastic model of the DEP system is assembled and nonlinear simulations are performed. The simulation results indicate that distributed propellers possess significant potential for wing vibration suppression and load alleviation. This modeling approach provides a numerical modeling and simulation for conducting subsequent multidisciplinary design and control research. In practical engineering, high-bandwidth electric motors are utilized not only as conventional thrust devices, but also as active aerodynamic effectors. Facilitating the development of active vibration suppression and gust load alleviation systems contributes to

achieving structural weight reduction, fatigue life extension, and significant improvements in flight safety for next-generation DEP aircraft.

Although the developed model achieves a balance between computational efficiency and the preservation of key physical mechanisms, its applicability is primarily limited to the linear attached-flow regime at low-to-moderate angles of attack. Under extreme operating conditions, several limitations remain that may affect its predictive accuracy. First, the aerodynamic formulation is based on potential flow theory, thereby neglecting viscous effects, flow separation at high angles of attack, and the complex viscous interactions between propeller slipstream and the wing boundary layer. As a result, in nonlinear flow regimes, the model tends to overpredict the lift coefficient while underestimating profile drag and separation-induced pressure drag. Second, although the slipstream tube model offers high computational efficiency, it significantly simplifies the inherently complex vortex interactions and distortions within the propeller wake.

Future research will be directed toward the following expansions:

1. Employing high-fidelity CFD simulations to quantitatively validate and calibrate the current reduced-order model.
2. Investigating active vibration control strategies specifically tailored for the DEP system, leveraging the rapid response and redundant control authority of multiple electric motors to suppress aeroelastic oscillations and mitigate the dynamic impact of engine failure scenarios.
3. Exploring the feasibility of randomizing propeller azimuth angles to achieve aeroelastic vibration mitigation by disrupting the spatial aerodynamic synchronization of rotor wakes and downwash, thereby suppressing the periodic aeroelastic vibrations and vertical displacement of the wing.

**Author Contributions:** Conceptualization, J.W. and Q.L.; methodology, J.W., W.G. and Q.L.; software, J.W. and W.G.; validation, J.W. and W.G.; formal analysis, J.W.; investigation, Q.L. and B.L.; resources, B.L.; data curation, J.W.; writing—original draft preparation, J.W.; writing—review and editing, W.G., B.L. and Q.L.; visualization, J.W.; supervision, Q.L.; project administration, B.L.; funding acquisition, Q.L. and B.L. All authors have read and agreed to the published version of the manuscript.

**Funding:** This research was sponsored by the Science and Technology Commission of Shanghai Municipality of China (24TS1401700 and 24TS1402000).

**Institutional Review Board Statement:** Not applicable.

**Informed Consent Statement:** Not applicable.

**Data Availability Statement:** The data presented in this study are available on request from the corresponding author.

**Conflicts of Interest:** The authors declare no conflicts of interest.

## References

1. Sehra, A.K.; Whitlow, W., Jr. Propulsion and power for 21st century aviation. *Prog. Aerosp. Sci.* **2004**, *40*, 199–235. [CrossRef]
2. Felder, J.; Tong, M.; Chu, J. Sensitivity of mission energy consumption to turboelectric distributed propulsion design assumptions on the N3-X hybrid wing body aircraft. In Proceedings of the 48th AIAA/ASME/SAE/ASEE Joint Propulsion Conference & Exhibit, Atlanta, GA, USA, 30 July–1 August 2012.
3. Fard, M.T.; He, J.; Huang, H.; Cao, Y. Aircraft distributed electric propulsion technologies—A review. *IEEE Trans. Transp. Electrif.* **2022**, *8*, 4067–4090. [CrossRef]
4. Kim, H.D.; Perry, A.T.; Ansell, P.J. A Review of Distributed Electric Propulsion Concepts for Air Vehicle Technology. In *Proceedings of the 2018 AIAA/IEEE Electric Aircraft Technologies Symposium (EATS)*; IEEE: Piscataway, NJ, USA , 2018; pp. 1–21.
5. Synodinos, A.; Self, R.; Torija, A. Preliminary noise assessment of aircraft with distributed electric propulsion. In Proceedings of the 2018 AIAA/CEAS Aeroacoustics Conference, Atlanta, GA, USA, 25–29 June 2018.

6. Sahoo, S.; Zhao, X.; Kyprianidis, K. A review of concepts, benefits, and challenges for future electrical propulsion-based aircraft. *Aerospace* **2020**, *7*, 44. [CrossRef]
7. Xia, J.; Zhou, Z. The Modeling and Control of a Distributed-Vector-Propulsion UAV with Aero-Propulsion Coupling Effect. *Aerospace* **2024**, *11*, 284.
8. Berton, J.J.; Haller, W.J. A noise and emissions assessment of the N3-X transport. In Proceedings of the 52nd Aerospace Sciences Meeting, National Harbor, MD, USA, 13–17 January 2014.
9. Posey, J.; Tinetti, A.; Dunn, M. The low-noise potential of distributed propulsion on a catamaran aircraft. In Proceedings of the 12th AIAA/CEAS Aeroacoustics Conference (27th AIAA Aeroacoustics Conference), Cambridge, MA, USA, 8–10 May 2006.
10. Burston, M.; Ranasinghe, K.; Gardi, A.; Parezanović, V.; Ajaj, R.; Sabatini, R. Design principles and digital control of advanced distributed propulsion systems. *Energy* **2022**, *241*, 122788. [CrossRef]
11. Carrier, G.; Atinault, O.; Grenon, R.; Verbecke, C. Numerical and experimental aerodynamic investigations of boundary layer ingestion for improving propulsion efficiency of future air transport. In Proceedings of the 31st AIAA Applied Aerodynamics Conference, San Diego, CA, USA, 24–27 June 2013.
12. Blumenthal, B.T.; Elmiligui, A.A.; Geiselhart, K.A.; Campbell, R.L.; Maughmer, M.D.; Schmitz, S. Computational investigation of a boundary-layer-ingestion propulsion system. *J. Aircr.* **2018**, *55*, 1141–1153. [CrossRef]
13. Laskaridis, P.; Pachidis, V.; Pilidis, P. Opportunities and challenges for distributed propulsion and boundary layer ingestion. *Aircr. Eng. Aerosp. Technol.* **2014**, *86*, 451–458. [CrossRef]
14. Wheeler, P.; Sirimanna, T.S.; Bozhko, S.; Haran, K.S. Electric/hybrid-electric aircraft propulsion systems. *Proc. IEEE* **2021**, *109*, 1115–1127. [CrossRef]
15. Amoozgar, M.; Dimitriadis, G.; Cooper, J.; Ajaj, R. Gust load alleviation of electric aircraft with distributed propulsors using thrust vectoring. In Proceedings of the International Forum on Aeroelasticity and Structural Dynamics, IFASD 2024, The Hague, The Netherlands, 17–21 June 2024.
16. Kilimtzidis, S.; Kostopoulos, V. Multidisciplinary structural optimization of novel high-aspect ratio composite aircraft wings. *Struct. Multidiscip. Optim.* **2023**, *66*, 150. [CrossRef]
17. Marcus, E.A.; de Vries, R.; Raju Kulkarni, A.; Veldhuis, L.L. Aerodynamic investigation of an over-the-wing propeller for distributed propulsion. In Proceedings of the 2018 AIAA Aerospace Sciences Meeting, Kissimmee, FL, USA, 8–12 January 2018.
18. Sinnige, T.; van Arnhem, N.; Stokkermans, T.C.; Eitelberg, G.; Veldhuis, L.L. Wingtip-mounted propellers: Aerodynamic analysis of interaction effects and comparison with conventional layout. *J. Aircr.* **2019**, *56*, 295–312. [CrossRef]
19. De Vries, R.; van Arnhem, N.; Sinnige, T.; Vos, R.; Veldhuis, L.L. Aerodynamic interaction between propellers of a distributed-propulsion system in forward flight. *Aerosp. Sci. Technol.* **2021**, *118*, 107009. [CrossRef]
20. Herzog, N.; Reeh, A.; Kümmel, A.; Breitsamter, C. Analysis of Distributed Electric Propulsion on Commuter Aircraft. In Proceedings of the AIAA Scitech 2021 Forum, Virtual, 11–15. 19–21 January 2021.
21. Raichle, A. Flux Conservative Discretization of the Actuator Disk Model as a Discontinuity Surface. Ph.D. Thesis, Technical University Braunschweig, Braunschweig, Germany, 2017.
22. de Rosa, D.; Morales Tirado, E.; Mingione, G. Parametric investigation of a distributed propulsion system on a regional aircraft. *Aerospace* **2022**, *9*, 176. [CrossRef]
23. Della Vecchia, P.; Malgieri, D.; Nicolosi, F.; De Marco, A. Numerical analysis of propeller effects on wing aerodynamic: Tip mounted and distributed propulsion. *Transp. Res. Procedia* **2018**, *29*, 106–115. [CrossRef]
24. Portillo, D.; Romero, I. Embedding structures in continua: Linear models and finite element discretizations. *Comput. Methods Appl. Mech. Eng.* **2026**, *451*, 118683. [CrossRef]
25. Cesnik, C.E.; Palacios, R.; Reichenbach, E.Y. Reexamined structural design procedures for very flexible aircraft. *J. Aircr.* **2014**, *51*, 1580–1591. [CrossRef]
26. Hesse, H.; Palacios, R. Reduced-order aeroelastic models for dynamics of maneuvering flexible aircraft. *AIAA J.* **2014**, *52*, 1717–1732. [CrossRef]
27. Wang, Q.; Siqueira, L.O.; Xu, T.; Cui, G.; Li, Z.; da Costa Azevêdo, A.S.; Picelli, R.; Xie, Y.M. Aerodynamics-driven topology optimization of compliant airfoils considering stability. *Comput. Methods Appl. Mech. Eng.* **2026**, *448*, 118454. [CrossRef]
28. Zúñiga, D.C.; Souza, A.G.; Góes, L. Flight dynamics modeling of a flexible wing unmanned aerial vehicle. *Mech. Syst. Signal Process.* **2020**, *145*, 106900. [CrossRef]
29. Waszak, M.R.; Schmidt, D.K. Flight dynamics of aeroelastic vehicles. *J. Aircr.* **1988**, *25*, 563–571. [CrossRef]
30. Guo, A.; Zhou, Z.; Zhu, X.; Zhao, X. Coupled flexible and flight dynamics modeling and simulation of a full-wing solar-powered unmanned aerial vehicle. *J. Intell. Robot. Syst.* **2021**, *101*, 56. [CrossRef]
31. Guimarães, T.A.; Cesnik, C.E.; Kolmanovsky, I.V. An Integrated Low-Speed Aeroelastic-Flight-Dynamics Framework for Modeling Supersonic Aircraft. In Proceedings of the AIAA SciTech 2022 Forum, San Diego, CA, USA, 3–7 January 2022.

32. Beyer, Y.; Cavaliere, D.; Bramsiepe, K.; Khalil, K.; Bauknecht, A.; Fezans, N.; Steen, M.; Hecker, P. An aeroelastic flight dynamics model for gust load alleviation of energy-efficient passenger airplanes. In Proceedings of the AIAA Aviation 2023 Forum, San Diego, CA, USA, 12–16 June 2023.
33. Böhnisch, N.; Braun, C.; Marzocca, P.; Muscarello, V. Impact of aerodynamic interactions on aeroelastic stability of wing-propeller systems. *Appl. Sci.* **2024**, *14*, 8709. [CrossRef]
34. Wu, X.; Zhou, Z.; Wang, Z. Rapid dynamic aeroelastic response analysis of the highly flexible wing with distributed propellers influence. *Aeronaut. J.* **2024**, *128*, 2668–2690. [CrossRef]
35. Sun, J.; Zhou, Z.; Tengis, T.; Fang, H. Analysis of Static Aeroelastic Characteristics of Distributed Propulsion Wing. *Aerospace* **2024**, *11*, 1045. [CrossRef]
36. Gao, Z.; Luo, H.; Shao, X.; Pan, D.; Zeng, L.; Wang, L. Meshless simulation of multi-propeller/wing interactions in typical distributed electric propulsion configurations. *Aerosp. Sci. Technol.* **2025**, *163*, 110287. [CrossRef]
37. Xue, C.; Zhou, Z. Propeller-wing coupled aerodynamic design based on desired propeller slipstream. *Aerosp. Sci. Technol.* **2020**, *97*, 105556. [CrossRef]
38. Lechniak, J.A. LEAPTech/HEIST experiment test and evaluation summary. In *Proceedings of the AIAA Aviation and Aeronautics Forum (Aviation 2018)*; NASA: Washington, DC, USA, 2018; p. AFRC-E-DAA-TN48263.
39. Truong, S.; Bhamidipati, K.; Lung, S.F.; Spivey, N.; Truax, R.; Winkel, J. X-57 Mod III Wing Ground Vibration Test. In *Proceedings of the IMAC XLIII*; River Publishers: Aalborg, Denmark, 2025.
40. Murua, J.; Palacios, R.; Graham, J.M.R. Applications of the unsteady vortex-lattice method in aircraft aeroelasticity and flight dynamics. *Prog. Aerosp. Sci.* **2012**, *55*, 46–72. [CrossRef]
41. Veldhuis, L.L. Review of propeller-wing aerodynamic interference. In *Proceedings of the 24th International Congress of the Aeronautical Sciences*; Optimage Ltd.: Edinburgh, UK, 2004; Volume 6, pp. 2004–2006.
42. Harder, R.L.; Desmarais, R.N. Interpolation using surface splines. *J. Aircr.* **1972**, *9*, 189–191. [CrossRef]
43. Katz, J.; Plotkin, A. *Low-Speed Aerodynamics*; Cambridge University Press: Cambridge, UK , 2001.
44. Dimitriadis, G. *Unsteady Aerodynamics: Potential and Vortex Methods*; John Wiley & Sons: Hoboken, NJ, USA, 2023.
45. Yu, S.; Zhou, X.; Huang, R. Time-varying aeroelastic modeling and analysis for a morphing wing. *AIAA J.* **2024**, *62*, 3825–3840. [CrossRef]
46. Vatistas, G.H.; Panagiotakakos, G.D.; Manikis, F.I. Extension of the n-Vortex Model to Approximate the Effects of Turbulence. *J. Aircr.* **2015**, *52*, 1721–1725. [CrossRef]
47. Simpson, R.J.; Palacios, R.; Murua, J. Induced-drag calculations in the unsteady vortex lattice method. *AIAA J.* **2013**, *51*, 1775–1779. [CrossRef]
48. Caradonna, F.X.; Tung, C. Experimental and analytical studies of a model helicopter rotor in hover. In *Proceedings of the European Rotorcraft and Powered Lift Aircraft Forum*; NASA: Washington, DC, USA, 1981; p. A-8332.
49. Doerffer, P.; Szulc, O. Numerical simulation of model helicopter rotor in hover. *TASK Q. Sci. Bull. Acad. Comput. Cent. Gdan.* **2008**, *12*, 227–236.
50. Verstraete, M.L.; Ceballos, L.R.; Hente, C.; Roccia, B.A.; Gebhardt, C.G. Code-to-code benchmark for simulation tools based on the unsteady vortex-lattice method. *J. Aerosp. Inf. Syst.* **2023**, *20*, 719–746. [CrossRef]
51. Veldhuis. Propeller Wing Aerodynamic Interference. Ph.D. Thesis, Delft University of Technology, Delft, The Netherlands , 2005.
52. Gao, W.; Liu, Y.; Li, Q.; Lu, B. Aerodynamic Modeling and Simulation of Multi-Lifting Surfaces Based on the Unsteady Vortex Lattice Method. *Aerospace* **2023**, *10*, 203. [CrossRef]
53. Nederlof, R.; Goyal, J.; Sinnige, T.; Ragni, D.; Veldhuis, L.L. Fast Numerical Modeling of Propeller–Wing Aerodynamic Interactions. *AIAA J.* **2025**, *63*, 2499–2519. [CrossRef]
54. Rwigema, M.K. Propeller blade element momentum theory with vortex wake deflection. In *Proceedings of the 27th International Congress of the Aeronautical Sciences*; Optimage Ltd.: Edinburgh, UK, 2010 ; Volume 1, pp. 727–735.
55. Hansen, M. *Aerodynamics of Wind Turbines*; Routledge: Abingdon, UK, 2015.
56. Alvarez, E.J.; Mehr, J.; Ning, A. FLOWUnsteady: An interactional aerodynamics solver for multirotor aircraft and wind energy. In Proceedings of the AIAA Aviation 2022 Forum, Chicago, IL, USA, 27 June–1 July 2022.
57. Stokkermans, T.C.; Van Arnhem, N.; Sinnige, T.; Veldhuis, L.L. Validation and comparison of RANS propeller modeling methods for tip-mounted applications. *AIAA J.* **2019**, *57*, 566–580. [CrossRef]
58. Moore, B. Principal component analysis in linear systems: Controllability, observability, and model reduction. *IEEE Trans. Autom. Control* **2003**, *26*, 17–32.


**Disclaimer/Publisher's Note:** The statements, opinions and data contained in all publications are solely those of the individual author(s) and contributor(s) and not of MDPI and/or the editor(s). MDPI and/or the editor(s) disclaim responsibility for any injury to people or property resulting from any ideas, methods, instructions or products referred to in the content.